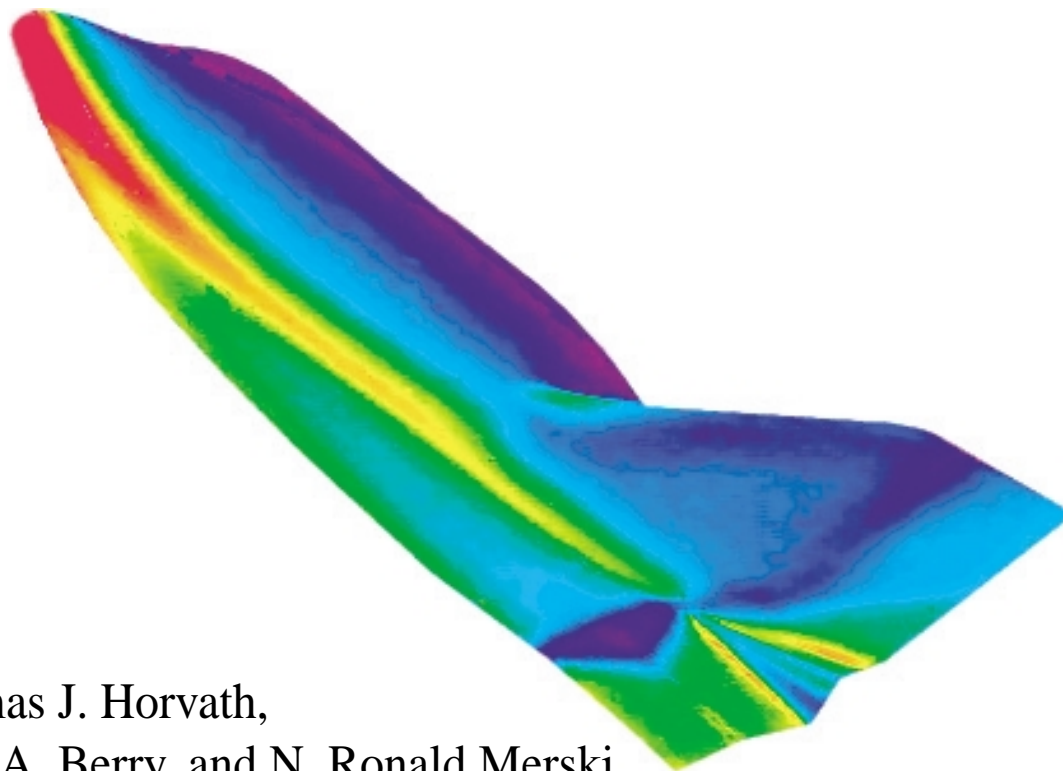




AIAA 2000-2685

X-38 Experimental Aerothermodynamics



Thomas J. Horvath,
Scott A. Berry, and N. Ronald Merski
NASA Langley Research Center
Hampton, Virginia

Steve M. Fitzgerald
NASA Johnson Spaceflight Center
Houston, Texas

**34th AIAA Thermophysics
Conference**

June 19-22, 2000 / Denver, CO

X-38 EXPERIMENTAL AEROTHERMODYNAMICS

Thomas J. Horvath*, Scott A. Berry*, N. Ronald Merski*[®]

NASA Langley Research Center

and

Steve M. Fitzgerald[†][®]

NASA Johnson Space Center

Abstract

The X-38 program seeks to demonstrate an autonomously returned orbital test flight vehicle to support the development of an operational Crew Return Vehicle for the International Space Station. The test flight, anticipated in 2002, is intended to demonstrate the entire mission profile of returning Space Station crew members safely back to earth in the event of medical or mechanical emergency. Integral to the formulation of the X-38 flight data book and the design of the thermal protection system, the aerothermodynamic environment is being defined through a synergistic combination of ground based testing and computational fluid dynamics. This report provides an overview of the hypersonic aerothermodynamic wind tunnel program conducted at the NASA Langley Research Center in support of the X-38 development. Global and discrete surface heat transfer, force and moment, surface streamline patterns, and shock shapes were measured on scaled models of the proposed X-38 configuration in different test gases at Mach 6, 10 and 20. The test parameters include angle of attack from 0 to 50 degs, unit Reynolds numbers from 0.3×10^6 to 16×10^6 /ft, rudder deflections of 0, 2, and 5 deg. and body flap deflections from 0 to 30 deg. Results from hypersonic aerodynamic screening studies that were conducted as the configuration evolved to the present shape are presented. Heavy gas simulation tests have indicated that the primary real gas effects on X-38 aerodynamics at trim conditions are expected to favorably influence flap effectiveness. Comparisons of the experimental heating and force and moment data to prediction and the current aerodynamic data book are highlighted. The effects of discrete roughness elements on boundary layer transition were investigated at Mach 6 and the development of a transition correlation for the X-38 vehicle is described. Extrapolation of ground based heating measurements to flight radiation equilibrium wall temperatures at Mach 6 and 10 were made and generally compared to within 50 deg F of flight prediction.

Nomenclature

b_{ref}	reference span (in)
h	heat transfer coeff. (lbm/ft ² -sec), $q/(H_{aw} - H_w)$ where $H_{aw} = H_{t,2}$
H	enthalpy (BTU/lbm)
L_{ref}	reference length (in)
M	Mach number
P	pressure, psia
q	heat transfer rate (BTU/ft ² -sec)
q	dynamic pressure (psi)
R	radius (in.)
t	time (sec)
Re	unit Reynolds number (1/ft)
S_{ref}	reference area (in ²)
T	temperature (°F)
X	axial distance from origin (in.)
Y	lateral distance from origin (in.)

α	angle of attack (deg)
δ	control surface deflection (deg)
ρ	density (lbm/in ³)
γ	ratio of specific heats
C_N	normal-force coefficient (N/ qS_{ref})
C_A	axial-force coefficient (A/ qS_{ref})
C_m	pitching-moment coefficient (m/ $qL_{ref}S_{ref}$)
$C_{l\beta}$	rolling-moment derivative (1/deg)
$C_{n\beta}$	yawing-moment derivative (1/deg)
$C_{y\beta}$	side-force derivative (1/deg)
L/D	lift to drag ratio

Subscripts

aw	adiabatic wall
BF	body flap
∞	free-stream conditions
n	model nose
$t, 1$	reservoir conditions
2	stagnation conditions behind normal shock
w	wall

* Aerospace Technologist, Aerothermodynamics Branch, NASA Langley Research Center, Hampton, VA.

[†] Aerospace Technologist, Aerosciences Branch, NASA Johnson Space Center, Houston, TX.

[®] Member, AIAA

Copyright ©2000 by the American Institute of Aeronautics and Astronautics, Inc. No copyright is asserted in the United States under Title 17, U.S. Code. The U.S. Government has a royalty-free license to exercise all rights under the copyright claimed herein for government purposes. All other rights are reserved by the copyright owner.

Introduction

The Crew Return Vehicle¹ (CRV) envisioned by NASA is intended to provide emergency return-to-earth capability from the International Space Station (ISS) in the event of medical or mechanical problems and Shuttle non-availability. Presently scheduled to be operational at the ISS in 2005, several CRV's are to be constructed by industry and delivered to the

station by the Shuttle. The X-38 program² led by NASA Johnson Space Center (JSC) seeks to fly a full-scale technology demonstrator to validate key design and operational aspects for the CRV. Conceived to demonstrate CRV technologies, the present X-38 design is considered flexible enough to evolve to a Crew Transfer Vehicle (CTV). The potential for CRV/CTV dual use has led to a cooperative NASA/European effort of the X-38 design^{3,4}. The CTV would be integrated to an expendable booster, such as the French Ariane 5, permitting personnel to be ferried to and from the station.

In the near term, the X-38 CRV technology demonstrator mission planned for 2002 calls for a 28.5 ft long vehicle (designated as V201) to be released from a Shuttle that is positioned in a high inclination ISS orbit. Following the jettison of a deorbit engine module, the X-38 will return unpowered (similar to the Space Shuttle) and then use a steerable parafoil⁵, a technology first developed by the Army, for its final descent. Landing will be accomplished on skids rather than wheels.

Consistent with the X-38 program's goal to take advantage of available equipment and technology to reduce vehicle development costs by an order of magnitude^{6,7}, the shape of the X-38 draws upon a synthesis of work performed by the U.S. government and industry over the last few decades^{8,9}. The initial X-38 shape (sketched in Fig.1 at 0.0295 scale) proposed by NASA JSC was based upon a lifting body concept originally developed and flown during the U.S. Air Force's PRIME (X-23/SV-5D)^{10,11} and PILOT (X-24A)¹² projects in the mid-1960s and early 70's. Referred to as Rev 3.1, this lifting body configuration was initially selected by JSC for the CRV mission due to its relatively high hypersonic L/D (higher L/D translates to larger cross range capability and shorter loiter times in orbit) and volumetric efficiency (room for all station crew if necessary). The current shape (Rev 8.3) departs from the X-23/X-24A and the initial Rev 3.1 in that it reflects changes to the vehicle upper surface to accommodate a vehicle capable of a CTV mission should the agency and its international partners decide to pursue this option. High approach speeds and long rollout distances associated with the low subsonic L/D from this lifting body requires that the landing be augmented with a steerable parafoil¹³. Critical for injured or incapacitated crew, this method permits the CRV to land within close proximity of medical facilities with minimal g-loads.

Under the NASA/European partnership, Dassault Aviation serves as prime contractor for the development of an X-38 Aerodynamic and Aerothermodynamic databases^{14,15}. The role of the NASA Langley Research Center (LaRC) Aerothermodynamics Branch (AB) has been to provide

hypersonic laminar and turbulent global surface heating and force and moment (F&M) data for CFD validation and as a cross check of X-38 data obtained in European facilities. Results from early LaRC wind tunnel heating tests on the initial Rev 3.1 compared favorably to CFD computations^{16,17}. Transition data was obtained¹⁸ which could be compared to similar measurements made on the Shuttle¹⁹ to support the use of a Re_{θ}/M_e criteria¹⁵ for assessment of manufacturing (step) tolerances of the Thermal Protection System (TPS) tiles. Hypersonic aerodynamic screening studies on Rev 3.1 were conducted at LaRC to assess the potential for real gas effects²⁰. Since the time of these publications, additional aerodynamic and aeroheating tests have been completed which include design changes to the vehicle outer mold lines. For complex thermal design environments on the X-38 (e.g. region behind split deflected body flaps), the original database has been supplemented. In this area, LaRC wind tunnel data in the form of discrete measurements has served as the primary source of heating information.

The purpose of this paper is to present an overview of the LaRC AB experimental program to characterize the X-38 hypersonic aerothermodynamic environment. As discussed in Ref. 21, the term "aerothermodynamics" is taken to encompass aerodynamics, aeroheating, and fluid dynamics. The experimental results were obtained in the LaRC Aerothermodynamic Facilities Complex (AFC)²². Over 1400 tunnel runs from 16 different entries in 4 facilities have been completed since May 1996. Table 1 lists of all the LaRC wind tunnel tests to date in support of X-38 aerothermodynamics. In terms of Mach and Reynolds number simulation, the most current X-38 flight trajectory (designated as Cycle 8) considered by NASA JSC (Fig. 2) has indicated that the 28.5-ft long flight vehicle would experience length Reynolds numbers (Re_L) of approximately 0.7×10^6 , 3.6×10^6 , and 6×10^6 at freestream Mach numbers of 20, 10, and 6 respectively. Fig. 2 also indicates the corresponding range of length Reynolds number that can be produced in the AFC with an appropriately sized models for each facility. Prediction along the current flight trajectory would place peak heating to the stagnation point of a reference sphere near Mach 23 at $\alpha=40$ deg.

Test techniques that were utilized during these tests include thermographic phosphors and thin film thermometry, which provide global and discrete surface heating respectively; oil-flow, which provides surface streamline information; schlieren, which provides shock details; and a six component strain gage balance to provide aerodynamic force and moment loads. Parametrics from the tests conducted in 4 facilities were Mach numbers of 6,10, and 20, normal shock density ratios of 4 to 12 produced in

three test gases; a range of angle of attack, 0 to 50 deg.; unit Reynolds number of 0.3 to 16 million/ft); and body flap deflections from 0 to 30 deg in 2.5 deg increments.

Experimental Methods

Models

The evolution of the X-38 Outer Mold Lines (OML) to the present shape (Rev 8.3) is highlighted in Fig. 3, a photograph of the various 0.0175 model scale force and moment models. All proposed vehicle configurations have incorporated symmetric fins with deflectable rudders and two body flaps that deflect away from the windward fuselage for aerodynamic control. The progression of OML modifications shown (Rev 3.1, YPAIO, and Rev 8.3) are indicative of changes made to the upper surface (or leeside); the windward surface has essentially retained the same basic shape as the SV-5D lifting bodies flown in the 1960's. Two basic model lengths (6 and 10-inch), determined by facility test core size, yielded model scale factors of 0.0175 and 0.0295.

As the LaRC test results were to provide benchmark data, model mold line accuracy relative to the CFD surface grid definition was important. This type of quality control was also necessary due to the complimentary tests conducted in Europe on separate models. To assure precision, numerically controlled milling machines were utilized in the fabrication of the X-38 family of force & moment wind tunnel models utilizing CAD geometry supplied by JSC. Rapid prototyping/casting techniques^{23, 24} were used for construction of the heat transfer models to provide an early assessment of the heating environment.

Forces and moments: Initial aerodynamic screening studies on X-38 conducted in the unheated 22-in Mach 20 Helium tunnel utilized resin SLA models for testing as temperature was not an issue. Two 6-in. (0.0175 scale) resin models were fitted internally with a steel sleeve in order to accept a balance. The models were designed to accept body flaps of various deflections.

Later studies on Rev 3.1 and Rev 8.3 conducted in the heated tunnels of the Aerothermodynamic Facilities Complex required the use of metallic models. The bodies of these two 6-in. models (Rev 3.1 and Rev 8.3) were fabricated from aluminum while the nose, fins, and control surfaces were 15-5 stainless steel. As with the earlier resin models, the metallic models incorporated multiple control surface settings, and internally fitted with interchangeable steel sleeves to accept several different balances.

Heat transfer: Two types of heat transfer models were fabricated: (1) a series of cast silica ceramic models for global information and (2) two

thin film models providing discrete measurements. At LaRC, the global phosphor technique has largely replaced the thin film technique due to the dramatic reduction in model fabrication time and instrumentation costs. While these benefits are revolutionary, the technique can have limitations where fast (sensor) response times are desired or the optical view of the model surface is limited. In the present X-38 heating studies, the required optical view behind the deflected body flaps was limited. Thin film instrumentation was used to compliment the global technique during this phase of testing.

Global phosphor thermography: Over 40 cast ceramic models were fabricated in support of the LaRC X-38 aerothermodynamic program, all of which share a common construction technique. A rapid prototyping technique was first used to build a resin stereolithography (SLA) model with various, detachable body flaps on both the port and starboard region of the base of the vehicle. The SLA resin model was then assembled with the desired control surface settings and served as a pattern to construct molds from which the cast ceramic model configurations were made. A magnesia ceramic was used to backfill the ceramic shells, thus providing strength and support to the sting support structure.

A photograph of six ceramic 0.0295 scale (10-in.) Rev 3.1 model configurations with various body flap deflections are shown in Fig.4. Typically, two casts of each configuration were made; the primary being immediately prepared for testing and the backup shell held in reserve, in case of problems with the primary. In order to obtain accurate heat transfer data with the phosphor technique, the models are cast with a material with low thermal diffusivity and well defined, uniform, isotropic thermal properties. The phosphor coatings typically do not require refurbishment between runs in the wind tunnel and have been measured to be approximately 0.001 inches thick. Details concerning the model fabrication technique and phosphor coating can be found in Refs.18 and 24. Fiducial marks were placed on the model surface to assist in determining spatial locations accurately.

Once the phosphor testing was completed, the untested backup models were prepared (spray-coated and kiln fired with a thin black glazing) for use as oil-flow and schlieren models.

Discrete thin film: Two metallic models were constructed and fitted with a machinable ceramic insert instrumented on the surface with small resistance thermometers. The first model, cast with aluminum, was created from a mold that used a resin SLA model as a pattern. This SLA resin model was identical to the pattern used to construct the cast ceramic phosphor heating models. The second model was unique in the sense that it was the first rapid

prototype, selective laser sintered metallic model successfully tested in a LaRC wind tunnel. In contrast to the more conventional rapid prototyping techniques that utilize resins or wax to create a pattern from which the actual tunnel model is cast, this technique omits the intermediate step by “building” the model, layer by layer, using a metallic powder. Originally, this model was intended as a backup to the cast aluminum model. Surface verification measurements indicated that the laser-sintered model was superior to the cast aluminum model in terms of linear shrinkage. Based on these results it was decided to instrument and test this model as well.

A photograph of the 0.0295 scale (10-in.) Rev 8.3 thin film model installed in the Mach 6 air tunnel is shown in Fig.5. The Cavity region behind the deflected body flaps was instrumented (see Fig.5a inset) with thin film gages to characterize the local heating in a region with restricted optical access. Sixty-eight sensors were placed at predetermined locations on the Macor (trademark of Corning Glass Works) substrate, Fig.5b.

Facility Descriptions

The Aerothermodynamic Facilities Complex (AFC) consists of five hypersonic wind tunnels that represent two-thirds of the nation's conventional aerothermodynamic test capability. Collectively, they provide a wide range of Mach number, unit Reynolds number, and normal shock density ratio²². This range of hypersonic simulation parameters is due, in part, to the use of three different test gases (air, helium, and tetrafluoromethane), thereby making several of the facilities unique national assets. The AFC facilities are relatively small and economical to operate, hence ideally suited for fast-paced aerodynamic performance and aeroheating studies aimed at screening, assessing, optimizing, and benchmarking (when combined with computational fluid dynamics) advanced aerospace vehicle concepts and basic fundamental flow physics research.

20-Inch Mach 6 Air Tunnel: Heated, dried, and filtered air is used as the test gas. Typical operating conditions for the tunnel are: stagnation pressures ranging from 30 to 500 psia; stagnation temperatures from 760-deg to 1000-degR; and freestream unit Reynolds numbers from 0.5 to 8 million per foot. A two-dimensional, contoured nozzle is used to provide nominal freestream Mach numbers from 5.8 to 6.1. The test section is 20.5 by 20 inches; the nozzle throat is 0.399 by 20.5-inch. A bottom-mounted model injection system can insert models from a sheltered position to the tunnel centerline in less than 0.5-sec. Run times up to 15 minutes are possible with this facility for F&M and pressure measurements. For the heat transfer and

flow visualization tests, the model residence time in the flow is only a few seconds.

20-Inch Mach 6 CF₄ Tunnel: Heated, dried, and filtered tetrafluoromethane (CF₄) is used as the test gas. Typical operating conditions for the tunnel are: stagnation pressures ranging from 85 to 2000 psia, stagnation temperatures up to 1300R, and freestream unit Reynolds numbers from 0.01 to 0.3 million per foot. A contoured axisymmetric nozzle is used to provide a nominal freestream Mach numbers from 5.9 to 6.01. The nozzle exit diameter is 20 inches with the flow exhausting into an open jet test section; the nozzle throat diameter is 0.466-inch. A bottom-mounted model injection system can inject models from a sheltered position to the tunnel centerline in less than 0.5-sec. Nominal run time for F&M testing is approximately 20 seconds in this facility.

31-Inch Mach 10 Air Tunnel: Heated, dried, and filtered air is used as the test gas. Typical operating conditions for the tunnel are: stagnation pressures ranging from 150 to 1350 psia; stagnation temperatures from 1750-deg to 1850-degR; and freestream unit Reynolds numbers from 0.25 to 2 million per foot. A three-dimensional, contoured nozzle is used to provide nominal freestream Mach number of 10. The test section is 31 by 31 inches; the nozzle throat is 1.07 by 1.07-inch. A side-mounted model injection system can insert models from a sheltered position to the tunnel centerline in less than 0.5-sec. Run times up to 1.5 minutes are possible with this facility, although for heat transfer and flow visualization tests, the model residence time required in the flow is only a few seconds.

22-Inch Mach 20 Helium Tunnel: Heated or unheated, dried, purified, and filtered helium is used as the test gas. Typical operating conditions for the tunnel are: stagnation pressures ranging from 300 to 3300 psia; stagnation temperatures from 490-deg to 900-degR; and freestream unit Reynolds numbers from 2.5 to 22 million per foot. A contoured axisymmetric nozzle is used to provide a nominal freestream Mach numbers from 18.1 to 22.3. The nozzle exit diameter is 22 inches with the flow exhausting into an open jet test section; the nozzle throat diameter is 0.622-inch. A bottom-mounted model injection system can insert models from a sheltered position to the tunnel centerline in less than 0.5-sec. Run times up to 30 seconds are possible with this facility.

Test Conditions and Setup

Nominal reservoir and corresponding free stream flow conditions for the four tunnels are presented in Table 2. The freestream properties were determined from the measured reservoir pressure and temperature and the measured pitot pressure at the test section (or inferred from previous calibrations). Test

section wall static and pitot pressures were monitored if possible and compared to tunnel empty conditions to assess if model blockage effects existed. No significant differences in pitot pressure were measured and it was concluded that significant blockage did not exist. The ratio of projected model frontal area ($\alpha=40$ deg) to tunnel cross sectional area for the 0.0175 scale model was less than 0.1.

All heating and force and moment models were supported by a base mounted cylindrical sting with the exception of the two thin film, heat transfer models which were blade supported from the leeside. This was done to minimize possible support interference associated with the flap cavity measurements. Details of the X-38 ceramic heat transfer model installation in the NASA LaRC 20-Inch Mach 6 Air Tunnel can be found in ref 18.

Test Techniques

Forces and Moments: Aerodynamic force and moment loads were measured throughout the test program using several sting-supported, six-component, water-cooled, internal strain gage balances. Balance temperature was monitored using integrated water jacket thermocouples to ensure excessive thermal gradients did not develop during the run. Typically, the aerodynamic models were tested in the inviscid test core flow on the tunnel centerline. In the CF₄ tunnel, the model was located approximately 1.0-inches downstream of the nozzle exit and laterally displaced 4-inches from the tunnel centerline to avoid small disturbances that are characteristic in axisymmetric nozzles. Limited tests made with the model on tunnel centerline did not indicate any measurable effect on the aerodynamic characteristics of the present configuration over the range of angle of attack tested.

Phosphor Thermography: Advances in image processing technology which have occurred in recent years have made digital optical measurement techniques practical in the wind tunnel. One such optical acquisition method is two-color relative-intensity phosphor thermography²⁵⁻²⁷ which has been utilized in several aeroheating tests conducted in the hypersonic wind tunnels of NASA Langley Research Center.^{19,28,29} With this technique, ceramic wind tunnel models are fabricated and coated with phosphors that fluoresce in two regions of the visible spectrum when illuminated with ultraviolet light. The fluorescence intensity is dependent upon the amount of incident ultraviolet light and the local surface temperature of the phosphors. By acquiring fluorescence intensity images with a color video camera of an illuminated phosphor model exposed to flow in a wind tunnel, surface temperature mappings can be calculated on the portions of the model that are in the field of view of the camera. A temperature calibration of the system conducted prior to the study

provides the look-up tables that are used to convert the ratio of the green and red intensity images to global temperature mappings. With temperature images acquired at different times in a wind tunnel run, global heat transfer images are computed assuming one-dimensional semi-infinite heat conduction. The primary advantage of the phosphor technique is the global resolution of the quantitative heat transfer data. Such data can be used to identify the heating footprint of complex, three-dimensional flow phenomena (e.g., transition fronts, turbulent wedges, boundary layer vortices, etc.) that are extremely difficult to resolve by discrete measurement techniques. Because models are fabricated and instrumented more rapidly and economically, global phosphor thermography has largely replaced discrete heating instrumentation in Langley's AFC.

Thin Film: Thin film resistance gage were used to infer convective heating in the region behind the deflected body flaps. Standard mechanical deposition techniques³⁰ developed at LaRC were used to fabricate the 0.030-in. by 0.040-in. platinum sensing elements. Surface temperatures were integrated over time to determine the local heat transfer rate using the 1DHEAT code developed by Hollis³¹. Both analytical^{32,33} and numerical finite-volume heat transfer models are incorporated into this code. The analytical solutions are derived from one-dimensional, semi-infinite solid heat conduction theory with the assumption of constant substrate (model) thermal properties. When using the analytical option the inferred heating rates are empirically corrected for the effects of variable model thermal properties. For the present study, the uncertainty associated with variable wall thermal properties is believed to be minimal, particularly in the flap cavity region where surface temperature increases of 5 deg F or less were measured.

Flow Visualization: Flow visualization in the form of schlieren and oil-flow techniques, was used to complement the surface heating and force & moment tests. The LaRC 20-Inch Mach 6 air and CF₄ Tunnels are equipped with a pulsed white-light, Z-pattern, single-pass schlieren system with a field of view encompassing the entire test core. Images were recorded on a high-resolution digital camera, enhanced with commercial software and electronically placed into this report. The 31-Inch Mach 10 air and 22-Inch Mach 20 He Tunnels do not have schlieren systems.

Surface streamline patterns were obtained using the oil-flow technique. Backup ceramic models or the metallic force models were spray-painted black to enhance contrast with the white pigmented oils used to trace streamline movement. A thin basecoat of clear silicon oil was first applied to the surface, and

then a mist of pinhead-sized pigmented-oil drops was applied onto the surface. After the model surface was prepared, the model was injected into the airstream and the development of the surface streamlines was recorded with a conventional video camera. The model was retracted immediately following flow establishment and formation of streamline patterns, and post-run digital photographs were taken.

Data Reduction and Uncertainty

A 16-bit analog-to-digital facility acquisition system acquired flow condition data. Measured values of $P_{t,1}$ and $T_{t,1}$ are believed to be accurate to within ± 2 percent.

Heating rates were calculated from the global surface temperature measurements using one-dimensional semi-infinite solid heat-conduction equations, as discussed in detail in Ref. 27. As discussed in Ref. 27, the accuracy of the phosphor system measurement is dependent on the temperature rise on the surface of the model. For the windward side heating measurements, the phosphor system measurement accuracy is believed to be better than $\pm 8\%$, and the overall experimental uncertainty of the phosphor heating data due to all factors is estimated to be $\pm 15\%$. In areas on the model where the surface temperature rise is only a few degrees (i.e. leeside or flap cavity), the estimated overall uncertainty is on the order of $\pm 25\%$. Repeatability for the normalized windward centerline (laminar) heat transfer measurements was found to be generally better than $\pm 4\%$.

Based on the analysis of Refs. 27 and 34, the discrete thin film heat transfer measurements are believed to be accurate to within ± 8 percent. Repeatability for the cavity heat transfer measurements was found to be generally better than ± 2 percent.

In general, aerodynamic data was obtained in a descending alpha sweep during each run to minimize errors associated with balance heating at the more relevant hypersonic entry angles-of-attack. In CF_4 , two separate runs were required to complete an angle-of-attack sweep due to the short run time. The data was collected by a analog-to-digital data acquisition system and averaged over a one second interval for each angle of attack (model held at fixed angle of attack for approximately 5 sec). The raw data was transferred to a Hewlett-Packard 9000 computer for data reduction and storage. During data reduction, corrections for weight tares, sting deflections, and balance interactions were made.

The force and moment data measured at the balance electrical center has been transferred to a moment reference center located at 57 % along the model x-axis. The model outer mold lines were checked and transfer distances were inferred from

measurement by the surface verification laboratory. Table 3 lists the reference area and lengths used to calculate the aerodynamic coefficients.

Base pressure measurements were made but were only used to provide information to help assess potential interference effects that may be present due to the sting/support system. All axial force coefficients, C_A , are reported as uncorrected for base pressure.

The estimated uncertainty in the reported aerodynamic coefficients was determined and reported²⁰ using the small sample method presented by Kline and McClintok³⁵. Where appropriate, estimated errors in the aerodynamic coefficients are indicated on the figure legend symbols.

Prediction Method

X-38 heating computations for selected angles-of-attack and test conditions were performed by several organizations within the European computational community. An overview of the computational methodology for X-38 development has been provided in Refs.14 and15. Because of the broad range of CFD codes presently being used to provide wind tunnel predictions, it was considered impractical to present details associated with surface and volume grid topology, grid sensitivity studies, and turbulence models in this experimental overview paper. All comparisons to CFD predictions were obtained from the X-38 aerothermodynamic database managed by NASA JSC. Every attempt was made to provide an appropriate reference to the original source of each numerical solution if the work was published in the open literature. In some cases, a referencable document was not available, and these cases are listed as unpublished.

Results and Discussion

Preface

As an overview paper of NASA LaRC AB contributions to X-38 aerothermodynamics, this section will highlight some of the more relevant observations to date. Details of how the present results are integrated into the JSC/European X-38 design methodology can be found in Refs. 14 and 15. First, the early aerodynamic screening exercises are reviewed and the data compared to the SV-5D preflight database. The influence of Mach number, Reynolds number, and gamma (real gas effect) on X-38 hypersonic aerodynamics is discussed. Pitching moment data has been presented around a moment reference center located at 57% of the body (reference) length. The aerodynamic results are followed by a synopsis of both global and localized heating measurements including some boundary layer

transition results, and an extrapolation of wind tunnel measurement to flight. Flow visualization in the form of surface oil flows is presented when necessary to assist in the interpretation of both force and moment and surface heating data. Heating mappings and distributions are presented in normalized form. For the global images, a constant color bar maximum value was selected for data presentation (except where noted) to maintain consistency when viewing or comparing the images. On the contour scale, the colors tending towards red indicate areas of higher heating (temperatures) while the colors towards blue represent areas of lower heating. In areas where the local heating exceeded the selected maximum color bar value, such as the deflected body flaps or fin leading edges, a gray “overscale” will be evident.

Aerodynamics

The initial hypersonic screening conducted in the Mach 20 Helium tunnel focused on the rapid aerodynamic assessment of a modified SV-5D vehicle shape (Rev 3.1) using stereolithography (SLA) models. Parametrics were confined to modifications to the vehicle leeside and fin leading edges and as expected, produced no measurable effects on longitudinal aerodynamics at entry angles of attack (not shown). The Helium tests were then expanded in scope to evaluate control surface effectiveness over a range of body flap deflections and to permit comparison to the PRIME SV-5D preflight wind tunnel database³⁸ (comparison of the Mach 20 Helium aerodynamic coefficients with computational prediction is presented in Ref. 17). While real gas effects on aerodynamics were not simulated in the present laminar Helium test results at Mach 20, the vehicle trim characteristics and L/D are in close agreement with values incorporated into the 1960’s database as shown, Fig. 6a-b. This agreement with the SV-5D database was not surprising as real gas effects were never quantified and incorporated into the original SV-5D preflight aerodynamic database. From a facility perspective, the quantification of real gas effects on aerodynamics was in its infancy, and predictive tools were not yet available during the original SV-5D development.

The role of LaRC in X-38 aerodynamic testing was broadened to include tests in other LaRC facilities (e.g. Unitary Plan Wind Tunnel, 16-foot Transonic Tunnel, and the Low Speed Spin Tunnel) to compliment tests conducted in Europe. In the hypersonic regime, the focus of this overview paper, the Rev 3.1 configuration was found to be longitudinally stable; trimming hypersonically at $\alpha = 40$ deg with approximately 15 deg body flaps and a corresponding L/D = 0.9. This configuration also exhibited positive directional control across the measured angle-of-attack range ($10 < \alpha < 50$ deg.). The effect of the primary simulation parameters on longitudinal aerodynamics (C_A , C_N , and C_m) was

performed by testing of the same model/balance/support system combination in the LaRC AFC. Viscous effects (Reynolds number) associated with a laminar boundary layer were determined at Mach 6. Compressibility effects (Mach number) were determined with comparisons of Mach 6 and 10 air data. Similarly, comparison of aerodynamic measurements between Mach 6 air and CF_4 , provided an indication of the significance of real gas effects for X-38 through the variation in normal shock density ratio produced with the two test medium.

The effects of Reynolds number on Rev 3.1 longitudinal aerodynamics at Mach 6 for 25 deg body flap deflection is presented in Figs 7. Normal force, Fig. 7a, coefficient remained essentially unchanged over the Reynolds number range while pitching moment, Fig. 7c, indicated a nose-down increment with increasing Reynolds number which suggested enhanced flap effectiveness. As Reynolds number was increased, it was found that the extent of separated flow on the control surface (as inferred from surface oil flow visualization-not shown) decreased as was indicated by the forward movement of the reattachment line on the flap. The presence of flow separation in the vicinity of the deflected control surfaces at all Reynolds numbers suggested a turbulent flow was not obtained at these tunnel conditions and a limiting case for flap effectiveness was not achieved (balance load limits were exceeded at higher Reynolds numbers). For Mach 6 flight it is anticipated that boundary layer upstream of the control surfaces will be turbulent which may further improve flap effectiveness relative to the laminar wind tunnel results. The decrease in axial coefficient, Fig. 7b, can be attributed to the expected decrease in skin friction with increasing Reynolds number. At incidence angles more typical of hypersonic entry, crossrange performance in terms of L/D (not shown) was essentially unaffected over this same laminar Reynolds number range.

Compressibility effects on Rev 3.1 laminar longitudinal aerodynamics, particularly at hypersonic entry angles-of-attack, were generally within the experimental uncertainty of the measurements (Fig. 8) with the exception of the Mach 20 axial coefficient (Fig. 8a) obtained in the Helium Tunnel. The low Mach 20 values of C_A relative to Mach 6 and 10 are more likely due to the factor of 6 difference in Reynolds number between the Mach 6 and 10 air data and the Mach 20 Helium tunnel than a compressibility effect. In terms of pitching moment, Fig. 8c, it is interesting to note a slight crossover in the coefficient between Mach 6 and 10 near $\alpha = 35$ deg. This same trend has been observed both experimentally³⁹ and computationally⁴⁰ within the X-33 program. While a variety of suggestions⁴¹ have been offered to explain this trend of decreasing

stability with decreasing Mach number, a consistent explanation has not been determined. It should be noted that these differences in X-38 C_m at Mach 6 and 10 are within the uncertainty of the measurement and more than sufficient control authority is produced by the deflected flaps to trim the vehicle.

It was recognized early in the X-38 development phase that, real gas effects were never quantified and incorporated into the original SV-5D preflight aerodynamic database. That is, high temperature effects due to dissociation could not be accurately determined (at that time) for the SV-5D basic body pitching moment and body flap effectiveness. Two decades later, the Shuttle Orbiter would experience a significant nose-up pitching moment increment relative to pre-flight predictions resulting in body flap deflections of twice the amount necessary to achieve trimmed flight. This phenomenon was later accurately simulated in the Langley CF_4 Tunnel and was coupled with computational methods to provide a high degree of confidence in estimating hypersonic entry aerodynamics⁴². It is commonly recognized today that the primary effect of a real gas on aerodynamics is to lower the specific heat ratio (γ) within the shock layer which in turn will produce a greater degree of flow compression and expansion relative to a perfect gas. Thus, expansion surfaces will have a correspondingly lower surface pressure. Because of the Shuttle experience and the presence of a windward expansion surface (boattail) on the aft end of the Rev 3.1 (with the flaps stowed at 0 deg deflection) it was suggested that aerodynamic real gas simulation testing (similar to that conducted on the Orbiter post-flight) be performed. The resulting aerodynamic measurements obtained in air and CF_4 at identical Mach and laminar Reynolds number, Fig.9, indicate that testing in a heavy gas (CF_4) resulted in small decreases in normal and axial force coefficients, Fig.9a-b, and a corresponding nose-up pitch increment for body flap deflection 0 deg, Fig.9c. This trend in the basic body pitching moment (neutral control surface deflection) was also noted in tests conducted on the Orbiter⁴².

The similarity in real gas trends between the X-38 and the Shuttle ended when the flaps were deployed. With the Shuttle, the relative nose-up increment between air and CF_4 persisted with the body flap deflected for trim⁴². This was not evident from the present X-38 Rev 3.1 test series which have indicated that for deflections larger than 15 degrees a relative nose-down increment in pitching moment was present, Fig. 9c. This is best explained when geometry differences of the respective windward surfaces are recognized. The Orbiter has a windward expansion surface that begins and coincides with the largest planform area; deflecting the body flap does not alter the expansion surface as the flap hangs off

the Orbiter base. In contrast, the X-38 flap hinge line is located farther forward on the body with the control surfaces deflecting away from the fuselage. Unlike the Orbiter, the windward expansion surface (boat-tail) found on the X-38 is effectively eliminated for body flap deflections greater than 15 deg. Thus, the primary real gas effects on X-38 aerodynamics at trim conditions are expected to influence flap effectiveness.

Relative to laminar perfect gas results the heavy gas simulation tests revealed an increase in body flap effectiveness across the angle-of-attack range, Fig.10. Real gas flight computations from Ref. 17 (not shown) for 25 deg body flap indicated higher pressure coefficients at the nose and body flap relative to perfect gas calculations. The pressure increase was more substantial at the flap and effected a larger area, which resulted in a net nose down increment. It is of interest to note that Ref. 10 has indicated that actual flight pressures on the SV-5D boattail expansion surface during hypersonic entry were lower than that obtained in wind tunnel tests, and that flight trim flap deflections were less than predicted by the preflight data base. The lower flight pressure on the boattail surface is consistent with a real gas effect and the increased body flap effectiveness in flight are consistent with trends observed from the present heavy gas wind tunnel tests and computational prediction. In general, the increments and trends provided by real gas simulation tests in air and CF_4 are applicable to flight provided that (1) the vehicle aerodynamics are dominated by the windward surface, (2) γ within the flight windward shock layer does not significantly vary spatially, and (3) γ within the flight windward shock layer is close in magnitude to that produced in CF_4 ($\gamma=1.1$).

Changes to the vehicle outer mold lines continued as the shape was optimized for performance across the speed range. These modifications have been confined to the leeside and it is assumed that these changes will not result in a significant departure from the real gas effects previously discussed. LaRC facilities have been utilized to assist in the evaluation of these changes on aerodynamics from transonic to hypersonic speeds. Tests at Mach 6 conducted on an interim OML designated YPAIO (between Rev3.1 and 8.3) revealed marginal lateral stability at lower incidence angles Fig.11a-c. In-situ model modifications resulted in a laterally stable vehicle across the angle-of-attack range. As expected, the addition of an ISS docking mechanism to the Vehicle (Rev 8.3) leeside did not produce any measurable effects in the longitudinal or lateral/directional aerodynamics (not shown) at Mach 6 for $15 > \alpha > 50$ deg.

The program has frozen the OML lines (Rev8.3) and is presently focusing efforts on developing and refining an aerodynamic design data book for flight. The most current X-38 Aerodynamic

Data Book ⁴³ (ADB-Rev G) provides a single source reference for all X-38 vehicle data appropriate to full scale flight performance. Aerodynamics in the data book up to Mach 10 are based on wind tunnel tests of various scale models tested in Europe. Included in the book are aerodynamic body flap control effectiveness data across the Mach range, which are presented in terms of increments from an undeflected state. Laminar body flap pitching moment increments, (ΔC_m), from LaRC tests at Mach 6 and 10 at a length Reynolds number of 1×10^6 are presented, Fig. 12a-b, along with the current ADB (Rev G) values. Differences between the LaRC results and the ADB (Rev G) are small and are believed to be within the uncertainties that will be allowed for by the X-38 flight control system.

Windward Surface Heating

Flight surface heating data from the SV-5D Precision Recovery Including Maneuvering Entry (PRIME) project of sufficient quality and quantity is not available for X-38 TPS design. The primary objective of the PRIME program was to demonstrate, through flight testing, lifting body aerodynamic performance during hypersonic entry at crossranges up to 700 miles. With the emphasis placed on aerodynamics, the flight program did not attempt to produce a large flight heating data base⁴⁴ (heating over most of the body was inferred from flight pressure measurements). Ground based tests conducted at the time proved to be sufficiently accurate for a conservative heatshield design¹¹. Lightweight ablative materials were used over the entire surface as anticipated heating conditions were considered to be more extreme than those expected for larger operational vehicles (such as the Shuttle flown almost 20 years later).

In terms of experimental and predictive methods, the aerothermodynamic community has progressed considerably since the development of the SV-5D vehicles. Up until the mid 1990's, however, aeroheating information for configuration assessment had continued to lag behind aerodynamic information due primarily to model and instrumentation complexities associated with aerothermodynamic testing. The X-38 program was able to take advantage of recent developments in the two-color global phosphor thermography technique, providing an opportunity to conduct an aerothermodynamic screening/trade study concurrent with aerodynamic tests. The aeroheating measurements from LaRC were primarily used in the continued development and validation of computational tools used to predict the X-38 aeroheating environment. Similar to the aerodynamic methodology of the program, the LaRC results were also intended to duplicate or compliment test results obtained in European facilities.

Fig. 13 illustrates a typical global comparison between experimental and numerically predicted laminar heating¹⁷ at wind tunnel conditions. The comparisons suggest a high level of confidence in the laminar numerical simulation over the acreage of the windward surface where the flow remains attached. Differences in the magnitude of the deflected flap surface heating and the apparent size of the separated flow upstream are indicative of a flow complexity that is more challenging to simulate numerically. Extracted heating distributions for this condition near the windward centerline and two axial stations are presented, Fig.14a-c, and are compared to laminar GASP prediction¹⁷. Measured centerline SV-5D heating data⁴⁵ from wind tunnel tests conducted at AEDC Tunnel C at Mach 10 and the Martin Hot Shot tunnel at Mach 20 over 35 years ago are also shown with the present LaRC Mach 10 results and prediction in Fig. 14a. Differences between the SV-5D data sets from Ref. 45 were noted at that time but were never resolved (while state of the art at the time, large uncertainties in the SV-5D data are presumed due to the nature of the thin skin calorimetry test technique). The SV-5D data sets bracket the present Mach 10 experimental and computational results. In retrospect, the SV-5D heating environment determined experimentally was adequate for a conservative TPS design. Modern quantitative global capabilities (experimental and computational) available today provide orders of magnitude more information in a fraction of the time permitting a less conservative design.

While primarily intended to provide data for computational validation, the LaRC tests were also intended to quantitatively assess the effects of Reynolds number, angle-of-attack, boundary layer transition, and configuration changes on heating. Subsonic/transonic aerodynamic optimization did lead to leeside OML changes and as a result some effort was devoted to the assessment of these changes on the heating environment. No significant issues regarding leeside heating (i.e. canopy, docking ring, or aft base flare) were identified experimentally.

On the windward surface, the influences of Reynolds number were most pronounced in the vicinity of the deflected flaps. Rev 3.1 windward heating at $M_\infty=6$, $\alpha=40$ deg and body flap deflection=25 deg are presented in Fig. 15 for a range of Reynolds number. The extracted longitudinal distributions are taken just off centerline so as to capture flapheating trends (heating to the cavity floor between the flap-split gap will be discussed at a later point). The collapse of the heating distributions with Reynolds number upstream of flap flow separation indicated the approaching flow was laminar. The corresponding windward global heating images and surface streamline patterns are shown, Fig. 16a-c and Fig.17a-c, respectively. Consistent with conclusions

inferred from the aerodynamic results, the extent of flow separation diminished with increasing Reynolds number. The flow reattachment downstream on the flap was observed to be in close proximity and nearly parallel to the 10 deg inboard swept flap hingeline. The flap hingeline gap is presently designed to be sealed to prevent circulation of this high-energy flow into the cavity. Tests are being planned to provide more detailed heating in this area. Near reattachment the streamlines are highly three-dimensional; inflow towards the flap split gap and expansion over the outboard flap edge was evident over the range of Reynolds numbers and at all angles-of-attack. The variation of heating levels on the flap with Reynolds number suggested a transitional/turbulent flow reattachment process. Flap heating will be discussed in more detail in a subsequent section.

Fin/Rudder Heating

The circulation of separated flow upstream of reattachment appeared to result in outboard flow spillage onto the nearby fin. Rev 8.3 heating images (note scale change), Fig. 18a-c, obtained at Mach 6 on the fuselage side ($\alpha=40$ deg, body flap deflection = 20 deg) indicated possible boundary layer transition of this entrained flow up onto the rudder surface. A comparison of extracted data along the fin chord in the vicinity of the rudder from the present tests with data from Ref. 45 is shown in Fig. 19. Boundary layer transition in the present tests has been inferred from the heating increase observed on the fin with increasing Reynolds number. Transitional/turbulent flow on the fin was not reported from the Mach 20 ground based wind tunnel test supporting the SV-5D development⁴⁵ and was likely due to boundary layer stabilization at high Mach number and low Reynolds number. Tripping of the flow with discrete roughness elements suppressed the measured fin heating, Fig. 20, from transitional to turbulent levels. When present, transitional heating on the fin rudder is 4 or more times the laminar value. A comprehensive numerical analysis of the heating in the rudder/fin gap⁴⁶ has indicated that a seal (or alternatively, an ablator material) may be required. In Ref. 46 it was shown that high heating on the rudder occurred at Mach 17.5 and 11 which conservatively assumed laminar and turbulent flow over the fin, respectively. The implications of transitional or turbulent flow at the higher Mach number have not been assessed. Additional LaRC tests at Mach 10 are planned to determine the susceptibility of the fin to boundary layer transition at Mach 10.

Windward Flap Heating

The thermal environment associated with the X-38 body flaps is considered to be a challenge from a design perspective due to the complex three-dimensional flowfield and resulting high surface temperatures anticipated in flight. The windward flap

temperatures in flight will be driven by several factors; three-dimensional flow separations, shear layer transition, multiple shock processing of the flow (bow, separation, reattachment), and flow expansion and acceleration over the flap edges and through the split gap. The X-38 flaps are designed as a hot structure⁴⁷ and will be manufactured from C/SiC, a ceramic matrix composite⁴⁸ (CMC). Early estimates of flap thermal loads suggested that CMC technology could provide an adequate thermal margin. Vehicle weight growth and trajectory refinements have significantly reduced this margin. A comprehensive computational and experimental effort has been initiated to more accurately predict the heating environment associated with the windward surface of the deflected body flaps and to insure this margin is not exceeded.

The peak heating to the deflected body flaps is largely determined by the state of the separated flow as it reattaches on the control surface. Three situations may arise: (1) laminar separation with laminar reattachment, (2) laminar separation with transitional or turbulent reattachment, and (3) turbulent separation with turbulent reattachment. Limited testing in Mach 10 with smaller scale Rev 3.1 heating models has suggested that laminar conditions prevailed at and downstream of flap reattachment. Comparison of the present LaRC Mach 10 heating extracted along the flap chord near the centerline ($\alpha=40$ deg, flap deflection of 20 deg) with laminar SV-5D data from Ref. 45 and unpublished laminar Navier-Stokes prediction from the CEVCATS code⁴⁹ is presented in Fig.21. The agreement with the experimental data from Ref. 45 is noteworthy considering the state of the art in instrumentation, signal conditioning, and data reduction in the 1960's. The laminar Navier-Stokes solution underpredicted the measured flap heating which has suggested that either the numerical simulation of the laminar flow separation and reattachment process was inadequately modeled, or that nonlaminar conditions prevailed in the Mach 10 ground based tests.

Laminar flap heating was not identified at Mach 6 for all Reynolds number conditions and it is believed that the flap heating was indicative of transitional or turbulent flow reattachment. The LaRC X-38 Rev 3.1 and 8.3 data was instrumental in developing flap heating augmentation and flight scaling factors for separating transitional or turbulent flows. The effects of flap deflection on Rev 3.1 global heating images obtained at Mach 6, $\alpha=40$ deg, and $Re_{\infty,L} = 2 \times 10^6$ are shown, Fig.22a-c. Extracted flap span heating distributions ($X/L=0.98$) are presented, Fig.23. The heating distributions along the body fuselage and flap chord ($y/b=0.2$) are shown, Fig.24, and correspond to the deflections shown in Fig. 23. The images at these conditions (as well as

all others) did not reveal the presence of Gortler vortices as is sometimes evident downstream of flow reattachment. This type of flow instability can produce heating augmentations of 30-50 percent above turbulent values and was a concern in the initial thermal design specifications of the flap. Extracted heating distributions along the flap span near the trailing edge (Fig. 23) were constant with the exception of the area near the flap split gap. An approximate increase of 15 percent in heating to the flap edge was measured and is the result of the inflow towards the gap (and inferred acceleration over the edge) observed in the streamline patterns presented earlier (Fig.17). Increasing the body flap deflection angle from 20 to 30 deg resulted in a 40 percent increase in overall heating levels on the flap downstream of reattachment. Closer to the point of flow reattachment ($X/L=0.9$), flap deflection had a more pronounced effect on heating as shown in Fig. 24. The “overshoot” in heating at reattachment for body flap deflections of 25 and 30 deg is characteristic of transitional flow. As observed with the fin heating, forced turbulence with discrete roughness elements placed upstream of separation suppressed the measured transitional heating on the flap, Fig. 25. The suppression of reattachment heating on the flap relative to transitional levels were also consistent with results obtained from heating studies conducted at AEDC on the SV-5D⁵⁰ (not shown).

Numerical prediction of transitional and turbulent interactions such as that which occurs with the X-38 deflected flap remains challenging. Turbulence models play a crucial role in the simulation of complex flows where separation, shock/boundary layer interaction, and flow reattachment are present. The correct prediction of surface heating depends to a large degree on the turbulence model. Predicted (published and unpublished) laminar and turbulent body and flap heating distributions from the CFD codes detailed in Refs. 49, 51, and 52 were compared to the measured LaRC Mach 6 heating data to develop a higher degree of confidence in predictive techniques utilized for X-38 flap design. The experimental heating distributions presented in Fig. 26a-b ($\alpha=40$ deg, body flap =20 deg, and $Re_{\infty,L} = 4 \times 10^6$) correspond to laminar and turbulent flow upstream of the deflected flap. The predicted laminar heating distributions from the two Navier-Stokes solvers^{49,51} and a two-layer method⁵² agreed with measured values and indicated the boundary layer upstream of flow separation was laminar, Fig. 26a. On the deflected flap, the measured heating was a factor of three higher than laminar predictions, which suggested non laminar flow reattachment (the two-layer method was not used to predict flap heating). Experimentally, the boundary layer was forced turbulent via discrete roughness and the resulting heating distribution

compared to turbulent prediction^{49,51,52}, Fig. 26b. As expected, the algebraic Baldwin-Lomax turbulence model⁵² did not perform well in the vicinity of the flap where an adverse pressure gradient and flow separation exist. A modified two-equation ($k-\omega$) turbulence model⁵¹ more accurately predicted the heating magnitude on the flap. The Shear Stress Transport (SST) turbulence model most faithfully reproduced the measured heating distribution on the deflected flap. While this comparison does not imply the turbulence model has been validated for flight, it does suggest that of the three numerical models investigated the SST may be the most suitable for application to X-38 flap design. Ref. 51 provides a detailed discussion of the numerical turbulence models, and comparisons to additional LaRC X-38 data and other benchmark experiments.

Flap Cavity Heating

The aerothermal environment of the cavity located behind the deflected flaps represents an extreme challenge from an experimental and numerical modeling perspective. In flight, forced convection through the flap gap, radiative heating between the flap leeside and aft cavity surfaces, flow separation, and three-dimensionality are all present. The presence of critical component hardware such as the flap actuator rod, Fig. 27, requires an accurate prediction of the environment to insure proper performance and adequate thermal protection. Experimentally, the cavity flowfield behind the flaps was dominated by the jet-like impingement of the flow through the flap split gap onto the cavity floor. A photograph of the surface streamline patterns from flow impingement at Mach 6, $\alpha=40$ deg, body flap =20 deg is shown, Fig. 28. The impingement produced longitudinal and spanwise variations in surface shear on the cavity floor.

To characterize the heating from the jet-like impingement, NASA LaRC provided the first detailed convective heating measurements made on the X-38 cavity surface. A comparison of Navier—Stokes unpublished laminar and turbulent prediction from the CFD code detailed in Ref. 51 with measured cavity floor heating at wind tunnel conditions ($\alpha=40$ deg, body flap =20 deg, and $Re_{\infty,L} = 4 \times 10^6$) is shown, Fig.29. For presentation purposes, the numerical solution on the left of the symmetry plane corresponds to turbulent flow ($k-\omega$) and on the right, laminar flow. The non-dimensional heating magnitudes from the discrete measurements (indicated within symbol) have been assigned color contour levels corresponding to that used for prediction. Similar to the phosphor results, the warmer colors (yellow, red etc) correspond to areas of higher heating. With the exception of the location of the cavity heating peak between the flap gap, the predictions captured the two-dimensional surface heating characteristics measured on the cavity floor. At this

Reynolds number condition it was determined experimentally that the heating peak to the cavity surface was located on centerline near the flap hingeline. In contrast, the computationally predicted peak was located near the vehicle trailing edge.

Additional experimental tests revealed that the heating peak to the cavity floor exhibited a strong spatial sensitivity to Reynolds number not predicted computationally. To visually capture global heating characteristics of the cavity floor from the discrete thin film measurements, the data obtained at Mach 6, $\alpha=40$ deg, body flap =25 deg are interpolated and presented in the form of a color contour plot, Fig. 30a-e. The forward movement of the heating peak toward the flap hingeline with increasing Reynolds number was observed. Secondary heating peaks were measured outboard of the centerline near the cavity vertical sidewall and corresponded to vortical flow inferred from the increase in shear in the surface streamline pattern, Fig. 28. The same data is replotted in a more conventional format, whereby centerline cavity normalized heating distributions are plotted vs. vehicle length (X/L), Fig. 31. The range of Reynolds numbers was sufficient to produce laminar and turbulent flow on the flap windward surface. The increase in magnitude and forward movement of the heating maximum on the cavity floor with Reynolds number coincided with the forward movement of flow reattachment (decreasing separation) on the windward flap surface. The magnitude increase and shift of the heating maximum with Reynolds number, were consistent with Mach 10 trends obtained from heating studies conducted at AEDC on the SV-5D⁵⁰ (this trend was observed with extreme flap deflections of 40 deg and consequently, not shown). A direct comparison of the SV-5D cavity centerline Mach 10 data of Ref. 50 with the corresponding LaRC Mach 6 X-38 heating distribution was possible for a flap deflection of 20 deg and is shown, Fig. 32. While the data from Ref. 50 was limited spatially (two thermocouples on the cavity floor), the heating maximum would appear to have been located near the aft end of the vehicle. This would be consistent with the present Mach 6 trends observed at low Reynolds number. The opening of a hinge line flap seal on the wind tunnel model of Ref. 50 appeared to have shifted the cavity-heating maximum forward towards the flap/cavity interface. Relief of the separated flow on the flap windward surface through the gap would appear to have produced a smaller recirculation region, emulating the high Reynolds number Mach 6 trends from the present test. Additional tests at higher Mach number ($M>6$) are required to determine if differences in the heating magnitude from the present test and Ref. 50 are due to compressibility effects. At equilibrium conditions during hypersonic entry, the cavity heating sensitivity to Reynolds number may not be as strong

as inferred from the perfect gas wind tunnel environment. The mechanism driving the cavity heating, flow separation on the flap windward surface would be less extensive in flight.

The effect of angle-of-attack and body flap deflection on cavity heating is presented, Figs. 33 and 34. Turbulent conditions on the flap windward surface prevail at this Reynolds number in the wind tunnel ($Re_{\infty,L} = 8 \times 10^6$) and are anticipated in flight at Mach 6. In contrast to the decreased heating on the windward flap surface, the lower flap deflections produced a more severe thermal environment on the cavity floor Fig 33. The effect of angle-of-attack on cavity heating at $Re_{\infty,L} = 8 \times 10^6$ for a fixed flap deflection of 25 degrees is shown in Fig. 34. Peak heating on the cavity behind the flaps approached 30 percent of reference stagnation values at 45 degrees angle-of-attack (Fig.34). Incidence angles of greater than 40 deg are presently being considered for hypersonic entry to moderate heating due to vehicle weight growth. It is reasonable to assume that the flap cavity interface may see significant heating if roll control authority requires flap deflections between 10 and 15 degrees at these higher entry angles-of-attack.

Currently, the design environment for this area has been compiled completely from LaRC experimental wind tunnel data. The measured heating distributions were invaluable in developing a thermal design model and flight scaling factors applicable to this localized region. Future computational work and experimental tests are anticipated to refine this model and reduce uncertainties.

Boundary Layer Transition

The proposed TPS of the X-38 windward surface consists of Shuttle-like ceramic tiles and similar to Orbiter flight experience, boundary layer transition is expected to be roughness dominated. Surface roughness may arise from inherent TPS tile mismatch due to manufacturing tolerances or may result from protruding gap filler material. An experimental effort¹⁸ was made to determine if X-38 boundary layer transition could be forced from discrete roughness. The analysis of data from Ref. 18 has been used to quantify the effects of isolated roughness along the centerline of the windward surface and to develop a transition correlation for the X-38 vehicle. Information from such a correlation has been used to provide manufacturing guidelines and constraints for the (step and gap) tolerances of the TPS tiles. With such step tolerances defined, an estimate of when boundary layer transition should occur in flight may be made.

The experimentally determined transition correlation was developed using the same methodology reported in Refs. 19 and 53. Phosphor heating images were used to identify the transition footprint located downstream of systematically placed roughness elements. The size and height of the

discrete tripping devices were methodically varied as was freestream unit Reynolds number in order to produce transitional and fully turbulent flow. Laminar boundary layer edge conditions at the trip location were computed by a boundary layer code⁵⁴ (LATCH) for a range of Reynolds numbers. To correlate the data, the experimental transition results were compared using the transition parameter of momentum thickness Reynolds number over edge Mach number (Re_{θ}/M_e) and the disturbance parameter of roughness height over boundary layer thickness (k/δ). Figure 35 provides the results of this correlation for all the discrete trip results along the X-38 centerline for Mach 6 at an angle-of-attack of 40 degrees. Curve fits representing transition onset, and fully turbulent flow have been experimentally determined for X-33⁵³ and are superimposed on the X-38 data set for comparative purposes. The correlated X-38 data are consistent with that determined for X-33. It is recognized that the determination of transition onset from discrete roughness can be influenced by tunnel noise⁵⁵ and that the incipient curve defined in Fig.35 may be conservative. The current X-38 TPS manufacturing guidelines specify step tolerances no larger than 0.08-in near the nose cap on the windward surface.

Extrapolation to flight

A feature of the phosphor thermography analysis package²⁶ (IHEAT) is the ability to extrapolate ground based heating measurements to flight radiation equilibrium wall temperatures. The successful application of this technique to predict Mach 6 flight surface temperatures for both laminar and turbulent conditions was demonstrated in the X-34^{26,27} and X-33²⁹ programs. Based on the successful Mach 6 extrapolation of X-33 and X-34 wind tunnel data and the good agreement between the X-38 measurement and prediction presented in this report, phosphor data were extrapolated to flight surface temperatures at Mach 6 and 10. Comparison of extrapolated data to turbulent Mach 6 and laminar equilibrium Mach 10 flight prediction are made, Figs. 36a-c and 37a-c. The Mach 6 tunnel data was obtained on Rev 8.3 at $\alpha = 40$ deg, flap deflection of 20 deg, and $Re_{\infty,L} = 4 \times 10^6$ where turbulence was forced with discrete roughness. Mach 6 flight conditions at $\alpha = 40$ deg correspond to an altitude of 127,000 ft., velocity of 6226 ft/s, and a length Reynolds number of 5×10^6 . The Mach 10 tunnel data was obtained on Rev 3.1 at $\alpha = 40$ deg, flap deflection of 25 deg, and $Re_{\infty,L} = 1 \times 10^6$. Mach 10 flight conditions at $\alpha = 40$ deg correspond to an altitude of 157,000 ft., velocity of 11,361 ft/s, and a length Reynolds number of 2.3×10^6 . No significant real-gas aeroheating effects were anticipated at the Mach 6 and 10 X-38 flight conditions.

The extrapolated phosphor images were mapped to the three-dimensional vehicle surface

geometry with the IHEAT code Map3D tool. The mapping technique permits a more accurate spatial representation of the global data particularly when extraction and comparison with numerical prediction are desired. The turbulent extrapolated surface temperatures at Mach 6 agreed quite well relative to predicted flight temperatures, Fig. 36a, with the exception of the body flap region. Consistent with the poor agreement found in the wind tunnel comparisons (Fig. 26b), the Baldwin-Lomax algebraic turbulence model used for the flight computation under-predicts the extrapolated (experimental) temperatures on the deflected body flap, as shown in Fig. 36b. Comparison of extrapolated temperature with turbulent prediction along an axial station well upstream of the expansion surface and deflected flaps, Fig. 36c, were in much better agreement.

The excellent comparison of laminar extrapolated temperature at Mach 10 to flight prediction, Fig. 37, illustrates the versatility of the extrapolation theory and has extended the demonstrated range of applicability to Mach 10. Similar to the Mach 6 data, the surface temperatures compared well over the entire image with the exception of the body flap. This again was not surprising as the extent of laminar separation was not captured computationally at wind tunnel conditions (see Fig. 13). Upstream of the flap interaction, the extrapolated wind tunnel data at Mach 6 and 10 generally compared to within 50 deg F (or better) of flight prediction. The extrapolation methodology has the potential to provide detailed and timely design information early in a design cycle, when a large number of vehicle parameters are being considered. This type of experimentally derived global information provided to the designer early in the TPS evaluation process would be invaluable for material selection and sizing requirements.

Concluding Remarks

The X-38 program plans to demonstrate an autonomously returned orbital test flight vehicle to support the development of an operational Crew Return Vehicle for the International Space Station that will return crew members safely back to earth in the event of medical or mechanical emergency. This report provides an overview of the hypersonic aerothermodynamic wind tunnel program conducted at the NASA Langley Research Center to date by the Aerothermodynamics Branch in support of the X-38 vehicle design.

The X-38 program was able to take advantage of recent developments in a two-color global phosphor thermography technique, providing an opportunity to conduct heating screening/trade study concurrent with aerodynamic tests. The LaRC ground based tests contributed significantly to the development and validation of the flight data book for

longitudinal and lateral aerodynamic characteristics as well as control surface effectiveness. Comparison of aerodynamic measurements between Mach 6 air and CF₄, provided an indication of the significance of real gas effects for X-38. Global and discrete surface heat transfer measurements were primarily used in the continued development and validation of computational tools used to predict the X-38 aeroheating environment. Under the present NASA/European partnership, the aerodynamic and heating measurements provided by LaRC were utilized to augment and compliment test results obtained in European facilities. The synergism between the experimental and computational work performed within the X-38 program has led to an improved understanding of complex flows.

The hypersonic aerodynamic wind tunnel tests indicated that the X-38 has more than sufficient control authority for pitch control. Pitching moment increments from the LaRC Mach 6 and 10 tests compared favorably with the data book values derived from European aerodynamic tests. The heavy gas simulation tests have indicated that the real gas effects on X-38 aerodynamics at trim conditions are expected to primarily influence flap effectiveness. Relative to laminar perfect gas results the heavy gas simulation tests revealed an increase in body flap effectiveness across the angle-of-attack range.

Global heating measurements for attached laminar flows were in good agreement with predictions from CFD codes used to define the flight aeroheating environment. Experimental heating measurements in the vicinity of control surfaces (body flaps and rudder) were made to provide initial design information from which thermal margin assessments were made. Predicted deflected flap heating distributions were compared to measured heating data from the LaRC tests in an effort to develop a higher degree of confidence in predictive techniques utilized for separating reattaching flows. Transitional flow reattachment represented a challenge from a numerical modeling perspective. In areas where predictive tools could not provide accurate information, such as the cavity behind the deflected flaps, the design environment has been compiled completely from LaRC experimental wind tunnel data. The heating distributions on the cavity floor were invaluable in developing a thermal design model and flight scaling factors applicable to this localized region. Future computational work and experimental tests are anticipated to refine this model and reduce uncertainties. A more comprehensive experimental and computational effort has been initiated to more accurately predict the flight-heating environment associated with the windward surface of the deflected body flaps.

The global aeroheating results obtained at Mach 6 have been used to quantify the effects of

isolated roughness along the centerline of the windward surface and to develop a transition correlation for the X-38 vehicle. Information from the correlation was used to provide manufacturing guidelines for the (step and gap) tolerances of the TPS tiles. With such step tolerances defined, estimates of when boundary layer transition would occur in flight can be made.

Extrapolation of ground based heating measurements to flight radiation equilibrium wall temperatures were made at Mach 6 and 10. The extrapolated wind tunnel data generally compares to within 50 deg F (or better) of flight prediction. This type of information provided to the designer early in the TPS evaluation process would be invaluable and could potentially result in significant savings of computational time required for flight predictions

Acknowledgments

Without the assistance of the following individuals this work would not have been possible: Mark Cagle, Joe Powers, Mike Powers, Mark Griffith, Ed Covington and Tom Burns for model design, fabrication, instrumentation, and surface inspection support; John Ellis, Rhonda Manis, Grace Gleason, Melanie Lawhorne, Harry Stotler, Steve Jones, and Jeff Werner for wind tunnel support; Sheila Wright and Bert Senter for data acquisition assistance; Tuan Trong, Leo Perez, Chuck Campbell, and Steve Labbe for analysis support; The German Aerospace Center (DLR) and the partners of the German national program on re-entry technologies, (TETRA) for CFD support; Dassault Aviation for the 2-Layer laminar and turbulent wind tunnel heating predictions; and Richard Wheless for documentation assistance. The authors gratefully acknowledge their contributions and behind-the-scenes work.

References

1. Brown, D., "Manning the Lifeboats on the International Space Station," *Launchspace*, April-May 1998, pp. 20-22.
2. Asker, J. R., "For Myriad of Woes, NASA Calls X-38 to the Rescue," *Aviation Week & Space Technology*, Nov. 11, 1996, pp. 70-71.
3. de Selding, P. B., "ESA, United States Advance Toward Common Crew Craft," *Space News*, Nov. 18-24, 1996, p.3.
4. de Selding, P. B., "Germany, NASA Pen Deal for Crew Lifeboat Work," *Space News*, Nov. 24-30, 1997.
5. Smith, B. A., "Weather May Hamper X-38 Drop Tests," *Aviation Week & Space Technology*, Dec. 8, 1997, p. 33.

6. Kandebo, S. W., "Vista F-16 Tests Preview X-38 Flight Controls" *Aviation Week & Space Technology*, Oct. 19, 1998, p. 41.
7. Covault, C., "Second X-38 Set for Flight" *Aviation Week & Space Technology*, Aug. 31, 1998, p. 58.
8. Reed, R. D. "Wingless Flight The Lifting Body Story," NASA SP-4220, 1997.
9. Barret, C., "Lifting Body Stability and Control," NASA TM -1999-209255, March 1999.
10. "SV-5D Prime Final Flight Test Summary," Martin Marietta Engineering Report ER 14465, Sept., 1967.
11. "Prime Follow-on Program: Addition Aerodynamic and Aerothermodynamic Data Analysis," Martin Marietta Engineering Report ER 14686, Jan., 1968.
12. Hallion, R.P., "The Hypersonic Revolution: Eight Case Studies in the History of Hypersonic Technology," Vol. 2, 1987, pp. 893-923.
13. Dornhiem, M. A., "X-38 Transitions from Lifting Body to Parafoil" *Aviation Week & Space Technology*, March, 23, 1998, p. 92.
14. Labbe, S. G., Perez, L.F., Fitzgerald, S. M., Longo, J. M. A., and Rapuc, M., "X-38 NASA/DLR/ESA-Dassault Aviation Integrated Aerodynamic and Aerothermodynamics Activities," Atmospheric Reentry Vehicle and Systems Symposium, Arachon, France, March 16-18, 1999.
15. Tribot, J. P., Tran, P., Pallegoix, J. F., Orłowski, M., Bruck, S., Andres, O. P., and Fitzgerald, S.M. "X-38 Aerothermodynamics," Atmospheric Reentry Vehicle and Systems Symposium, Arachon, France, March 16-18, 1999.
16. Campbell, C. H., Caram, J. M., Berry, S. A., Horvath, T. J., Merski, N. R., Loomis, M. P., and Venkatapathy, E., "An Overview of X-38 Hypersonic Aerothermodynamic Wind Tunnel Data and Comparison with Numerical Results," AIAA Paper 97-2475, 1997.
17. Loomis, M. P., Venkatapathy, E., Papadopoulos, P., Davies, C. B., Berry, S. A., Horvath, T. J., and Campbell, C. H., "Aeroheating and Aerodynamic CFD Validation and Prediction for the Computational/ Experimental Aeroheating Predictions for the X-38 Program," AIAA Paper 97-2478, June, 1997.
18. Berry, S. A., Horvath, T. J., Roback, V. E., and Williams, G. B., "Results of Aerothermodynamic and Boundary-Layer Transition Testing of 0.0362-Scale X-38 (Rev. 3.1) Vehicle in NASA Langley 20-Inch Mach 6 Tunnel," NASA TM-112857, September 1997.
19. Berry, S. A., Bouslog, S. A., Brauckmann, G. J., and Caram, J. M., "Shuttle Orbiter Experimental Boundary-Layer Transition Results with Isolated Roughness," *Journal of Spacecraft and Rockets*, Vol. 35, No. 3, 1998, pp. 241-248.
20. Campbell, C. H., Caram, J. M., Berry, S. A., Horvath, T. J., and DiFulvio, M., "Overview of X-38 Hypersonic Wind Tunnel Data and Comparison with Numerical Results," AIAA Paper 97-0567, January 1997.
21. Miller, C. G., "Development of X-33/X-34 Aerothermodynamic Data Bases: Lessons Learned and Future Enhancements," NATO Research and Tech. Org., Applied Vehicle Technology Symposium Aerodynamic Design and Optimization of Flight Vehicles in a Concurrent Multi-Disciplinary Environment, paper no. 32, Oct 1999.
22. Miller, C. G., "Langley Hypersonic Aerodynamic/Aerothermodynamic Testing Capabilities - Present and Future," AIAA Paper 90-1376, June 1990.
23. Buck, G. M., "Rapid Model Fabrication and Testing for Aerospace Vehicles," AIAA Paper 2000-0826, January 2000.
24. Buck, G. M. and Vasquez, P., "An Investment Ceramic Slip-Casting Technique for Net-Form, Precision, Detailed Casting of Ceramic Models," U. S. Patent 5,266,252, November 30, 1993.
25. Buck, G. M., "Automated Thermal Mapping Techniques Using Chromatic Image Analysis," NASA TM 101554, April 1989.
26. Merski, N. R., "Reduction and Analysis of Phosphor Thermography Data With the IHEAT Software Package," AIAA Paper 98-0712, Jan. 1998.
27. Merski, N. R., "Global Aeroheating Wind-Tunnel Measurements Using Improved Two-Color Phosphor Thermography Method" *Journal of Spacecraft and Rockets*, Vol. 36, No. 2, 1998, pp. 160-170.
28. Berry, S. A., Horvath, T. J., DiFulvio, M., Glass, C., and Merski, N. R., "X-34 Experimental Aeroheating at Mach 6 and 10," *Journal of Spacecraft and Rockets*, Vol. 36, No. 2, 1998, pp. 171-178.
29. Horvath, T. J., Berry, S. A., Hollis, B.R., Liechty, D.S., and Merski, N. R., "X-33 Experimental Aeroheating at Mach 6 Using Phosphor Thermography," AIAA Paper 99-3558, June, 1999.
30. Miller, Charles G. III, "Comparison of Thin-Film Resistance Heat-Transfer Gages With Thin-Skin Transient Calorimeter Gages in Conventional Hypersonic Wind Tunnels," NASA TM 83197.
31. Hollis, Brian R., "User's Manual for the One-Dimensional Hypersonic Experimental Aero-Thermodynamic (IDHEAT) Data Reduction Code," NASA CR 4691, (Grant Nos. NAG1-1663, NAGW-1331).
32. Cook, William J. , "Unsteady Heat Transfer Measurements to a Semi-Infinite Solid With

- Arbitrary Surface Temperature History and Variable Thermal Properties,” Iowa State Univ. Tech Report ISU-ERI-AMES-67500.
33. Kendall, D. N.; Dixon, W. P.; and Schulte, E. H., “Semiconductor Surface Thermocouples for Determining Heat-Transfer Rates,” *IEEE Transactions on Aerospace and Electronic Systems*, Vol AES-3, No. 4.
 34. Hollis, Brian R., “Experimental and Computational Aerothermodynamics of a Mars Entry Vehicle,” Phd Dissertation, North Carolina State University. (Grant Nos. NAG1-1663, NAGW-1331), 1996.
 35. Kline, S., and McClintok, F., “Describing Uncertainties in Simple Experiments,” *Mechanical Engineering*, pp. 3-8, 1953.
 36. AeroSoft, “GASP Version 3, The General Aerodynamic Simulation Program, Computational Flow Analysis Software for the Scientist and Engineer, User’s Manual,” AeroSoft, Inc., Blacksburg, VA., May 1996.
 37. Olynick, D. R., and Tam, T., “Trajectory Based Validation of the Shuttle Heating Environment,” *Journal of Spacecraft and Rockets*, Vol. 34, No. 2, 1997, pp. 172-181.
 38. F.C. Michel., “Aerodynamic Data Book- SV-5D Aerodynamic Characteristics. 680A Program,” CR-113 E, 5th Revision, Oct., 1, 1965.
 39. Murphy, K., Nowak, R., Thompson, R. A., and Hollis, B.R., “X-33 Hypersonic Aerodynamic Characteristics,” AIAA Paper 99-4162, August 1999.
 40. Hollis, B.R., Thompson, R. A., Murphy, K.J., Nowak, R.J., Riley, C.J., Wood, W.A., Alter, S.J., and Prabhu, R.K. “X-33 Aerodynamic and Aeroheating Computations for Wind Tunnel and Flight Conditions,” AIAA Paper 99-4163, August 1999.
 41. Thompson, R.A. “Review of X-33 Hypersonic Aerodynamic and Aerothermodynamic Development,” ICA 0323, August 2000.
 42. Brauckmann. G. J., Paulson, J. W., and Weilmuenster, J. K., “Experimental and Computational Analysis of the Space Shuttle Orbiter Hypersonic Pitch-Up Anomaly,” AIAA Paper 94-0632, January 1994.
 43. Perez, L., F., “X-38 Aerodynamic Design Data Book,” JSC-28854, Rev. G, Feb., 2000.
 44. Heppenheimer, T. A., “The Space Shuttle Decision. NASA’s Search for a Reusable Space Vehicle,” NASA SP-4221, 1999.
 45. Screen, E.N., and Nickel, H.S., “Hypersonic Heat Transfer Test Results From a 9.688% Model SV-5D Vehicle For Program 680A In the Martin Hypersonic Tunnel-Second Series,” ER-13686, Feb., 1965.
 46. Wong, H., Kremer, F., “Numerical Assessment on the Heating of the Rudder/Fin Gap in the X-38 Space Vehicle,” Atmospheric Reentry Vehicle and Systems Symposium, Arachon, France, March 16-18, 1999.
 47. Muhlrazer, A., Frohlich, A., and Wildenrotter, K., “Design, Material and Manufacturing Aspects of the X-38 Body Flaps,” Atmospheric Reentry Vehicle and Systems Symposium, Arachon, France, March 16-18, 1999.
 48. Trabandt U., Schmid, T., Reinkober, H., and Ritter, H., “Light-Weight CMC TPS for Future RLV Applied On X-38 Nose Skirt,” Atmospheric Reentry Vehicle and Systems Symposium, Arachon, France, March 16-18, 1999.
 49. Bruek, S., Radespiel, R., and Longo, J., “Comparison of Nonequilibrium Flows Past a Simplified Space-Shuttle Configuration,” AIAA Paocer 97-0275, Jan., 1997.
 50. Rhudy, R., and Merz, G., “Heat Transfer and Pressure Distribution on a Scale Model SV-5D at Mach 10,” AEDC-TR-194, September, 1965.
 51. Weber, C., Behr, R., and Weiland, C., “Investigation of Hypersonic Turbulent Flow Over the X-38 Crew Return Vehicle,” AIAA Paper 2000-2601, June 2000.
 52. Delattre, N., et al., “Numerical Prediction of Hypersonic Reacting Flows with the Finite Volume Solver FLU3NEQV,” AIAA Paper 97-0304, Sept., 1997.
 53. Berry, S. A., Horvath, T. J., Hollis, B.R., Thompson. R. A., Hamilton, H. H., “X-33 Hypersonic Boundary Layer Transition,” AIAA Paper 99-3560, June 1999.
 54. Hamilton, H., Green, F., and DeJarnette, F., “Approximate Method for Calculating Heating Rates on Three-Dimensional Vehicles,” *Journal of Spacecraft and Rockets*, Vol. 31, No. 3, 1994.
 55. Schneider, S. P., “Effects of High-Speed Tunnel Noise on Laminar-Turbulent Transition,” AIAA Paper 2000-2205, June, 2000.

Table 1: X-38 Aero/Aeroheating Tests in NASA LaRC AB Tunnels

Year	Tunnel	Test	Runs	Configuration(s)	Objective
1996	22-In Mach20 He	556	35	Rev 3.0/Rev 3.1	F&M Initial screening
1996	31-In Mach10 Air	322	42	Rev 3.0	Heating Initial screening
1996	22-In Mach20 He	560	20	YPAIO	F&M Revised OML
1996	20-In Mach6 CF4	113	56	Rev 3.1/YPAIO	F&M Gamma effects
1996	20-In Mach6 Air	6722	6	Rev 3.1	F&M Schlieren
1996	20-In Mach6 Air	6733	90	Rev 3.1/YPAIO	F&M Gamma effects
1996	20-In Mach6 Air	6735	174	Rev 3.1	Heating Transition
1997	31-In Mach10 Air	335	197	Rev 3.1/YPAIO	F&M Mach effects
1998	20-In Mach6 CF4	120	47	Rev 8.3	F&M Screening new OML
1998	20-In Mach6 Air	6765	50	Rev 8.3	F&M Screening new OML
1998	31-In Mach10 Air	345	122	Rev 8.3	F&M Mach effects
1998	20-In Mach6 Air	6774	138	Rev 8.3	F&M Gamma effects
1998	20-In Mach6 CF4	123	50	Rev 8.3	F&M Gamma effects
1998	20-In Mach6 CF4	125	143	Rev 8.3	F&M Gamma effects
1999	20-In Mach6 Air	6782	216	Rev 8.3	Heating Global/cavity
2000	31-In Mach10 Air	362	TBD	Rev 8.3	Heating Global/cavity

Table 2: Nominal Flow Conditions in NASA LaRC AFC Tunnels

Facility	M_∞	q_∞ (psi)	$P_{t,1}$ (psi)	$T_{t,1}$ (°F)	ρ_2/ρ_∞	Re_∞ /ft (x10 ⁶)
22-In Mach20 He	17.4	1.25	500	80	4.0	3.99
31-In Mach10 Air	9.7	0.66	350	1350	5.96	0.53
	9.83	1.25	720	1350	5.98	1.01
	9.95	2.41	1450	1350	5.98	2.00
20-In Mach6 Air	5.91	0.51	30	410	5.23	0.54
	5.90	1.04	60	430	5.23	1.04
	5.94	2.10	125	450	5.27	2.08
	5.98	4.07	250	450	5.28	4.06
	6.02	7.52	475	475	5.29	7.28
20-In Mach6 CF4*	5.98	0.80	950	850	11.68	0.35

*Mach 15-20 simulation due to high normal shock density ratio (ρ_2/ρ_∞) and/or low values of specific heat ratio (γ) within shock layer.

Table 3: X-38 Reference Dimensions

Dimension	Full scale (V201)	0.0175-scale
S_{ref}	233.28 ft ²	10.288 in ²
L_{ref}	27.6 ft	5.796 in
b_{ref} (= L_{ref})	27.6 ft	5.796 in
Moment reference center 0.57 x L_{ref}	15.732 ft	3.304 in

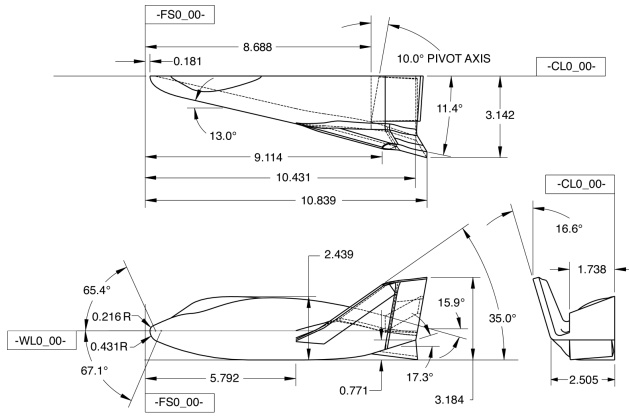


Figure 1. Dimensions (in inches) for 0.0295-scale X-38 Rev-3.1.

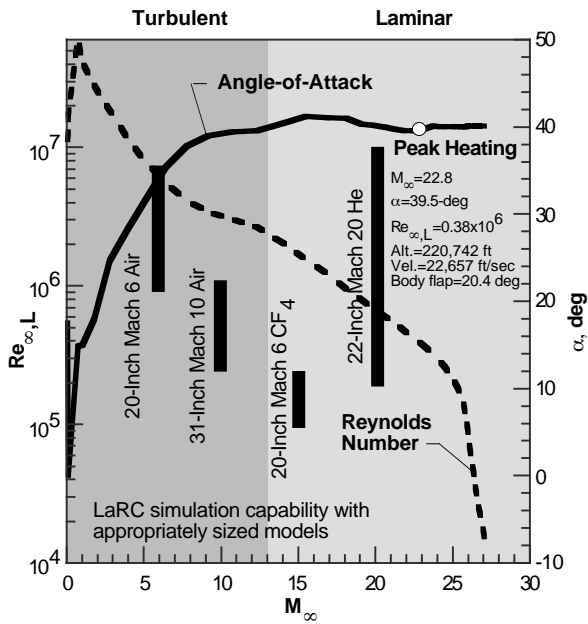


Figure 2. X-38 cycle 8 trajectory.



Figure 4. 0.0295-scale ceramic heat transfer models.

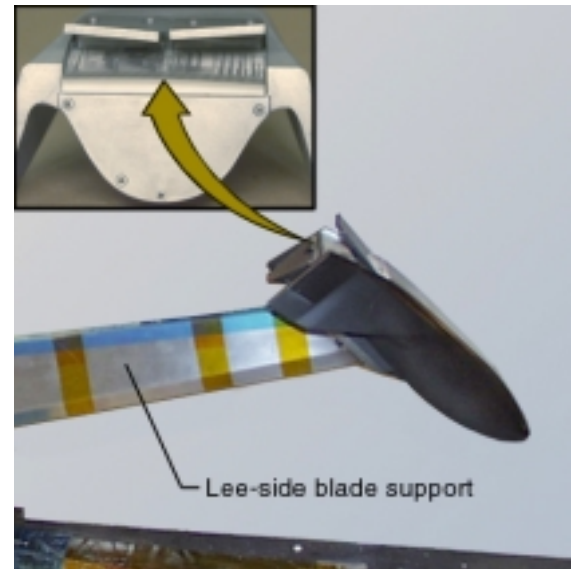


Figure 5a. Thin-film heat transfer model installed in the NASA LaRC 20-Inch Mach 6 Air Tunnel.

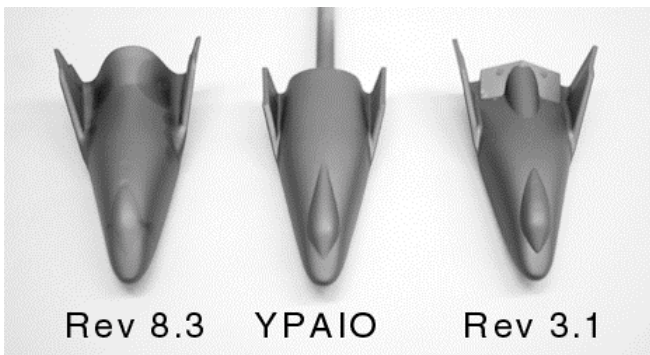
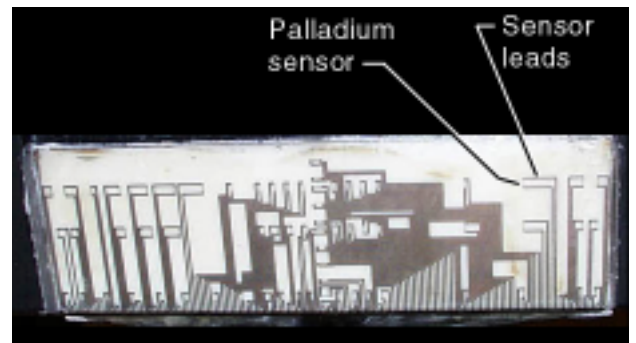
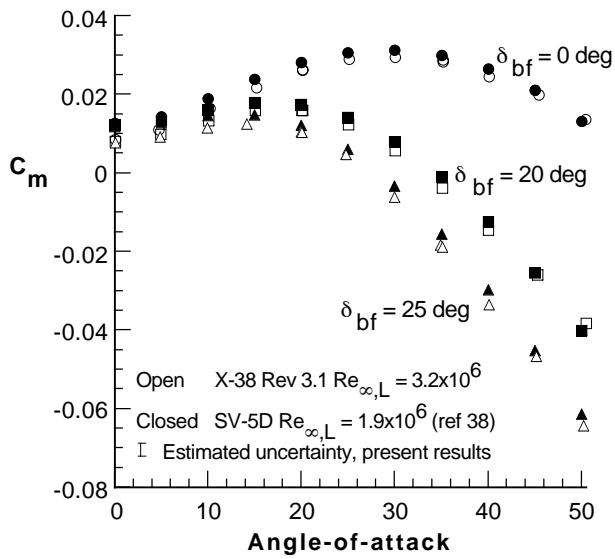


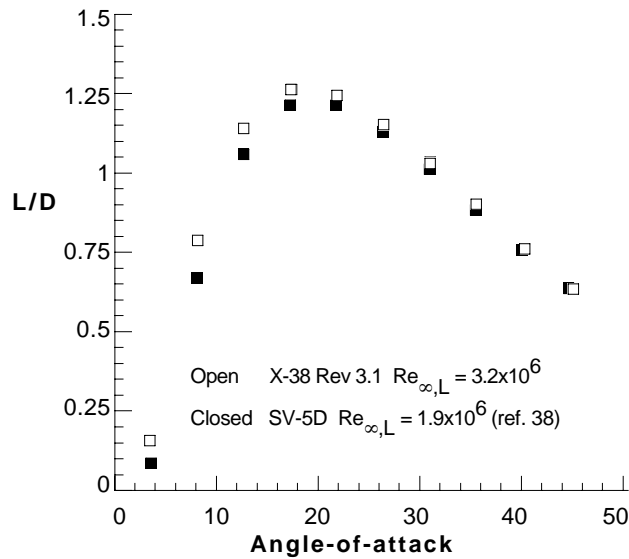
Figure 3. 0.0175-scale metallic force & moment models.



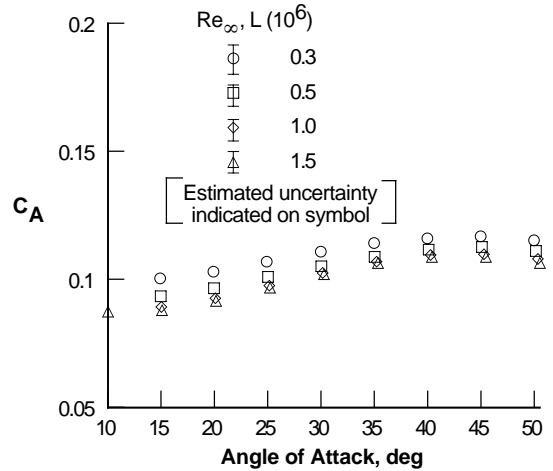
(b) Flap cavity thin film heat transfer sensors.



(a) Pitching moment coefficient, $M_\infty = 20$ Helium.
 Figure 6. Comparison of X-38 Rev 3.1 aerodynamics to SV-5D preflight database (ref. 38).

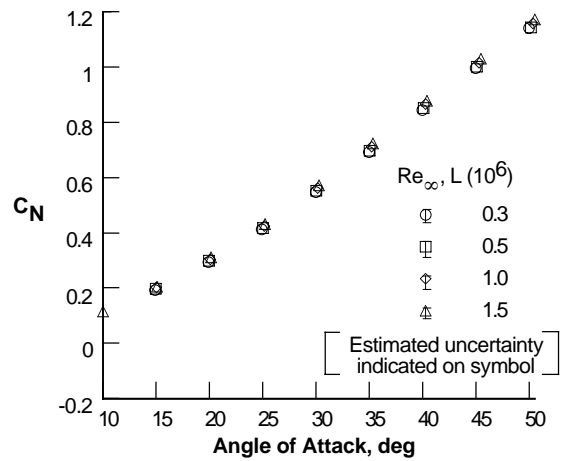


(b) Lift-to-drag ratio, $M_\infty = 20$ Helium, $\delta_{BF} = 20$ deg.

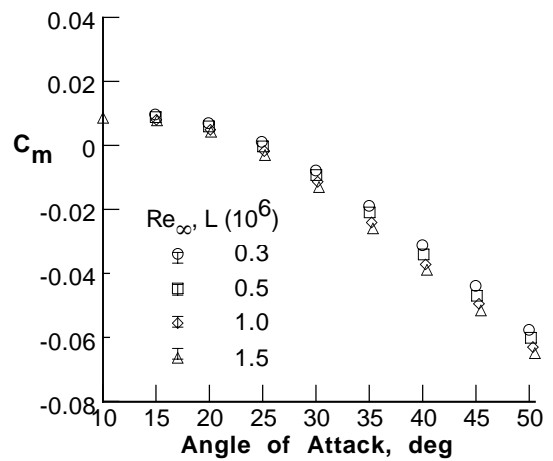


(a) Axial force coefficient.

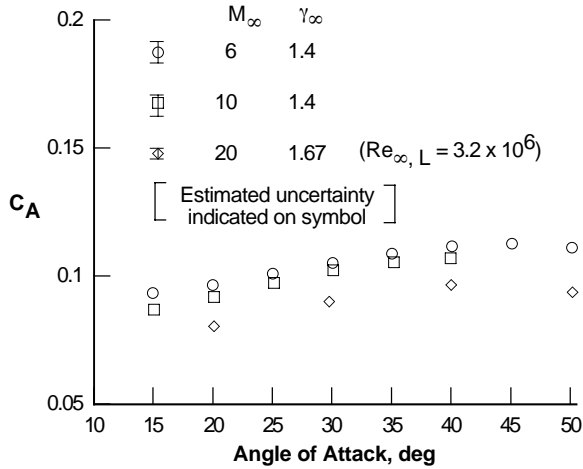
Figure 7. Reynolds number effects on X-38 Rev 3.1 longitudinal aerodynamics $M_\infty = 6$ air, $\delta_{BF} = 25$ deg.



(b) Normal force coefficient.

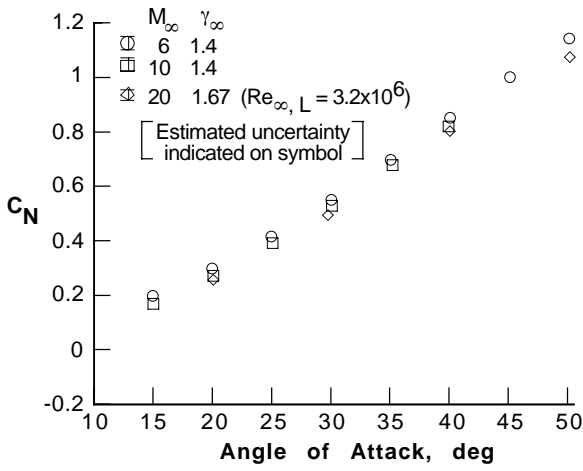


(c) Pitching moment coefficient.

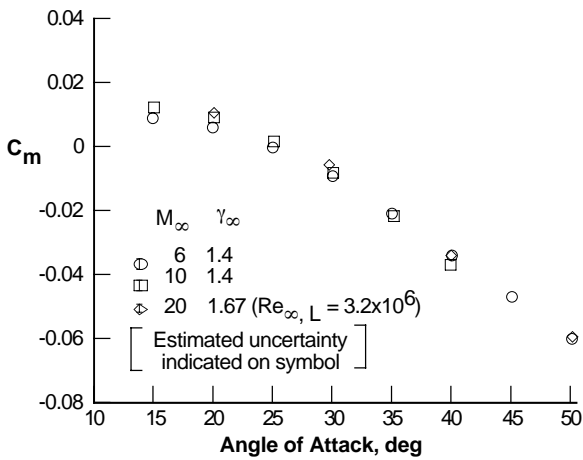


(a) Axial force coefficient.

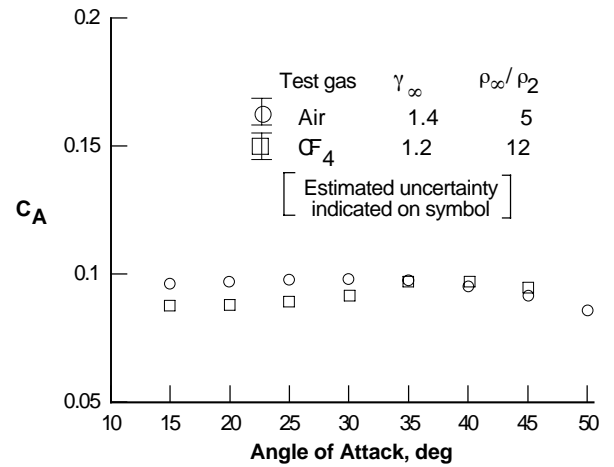
Fig. 8. Mach number effects on X-38 Rev 3.1 longitudinal aerodynamics $Re_{\infty, L} = 0.5 \times 10^6$, $\delta_{BF} = 25$ deg.



(b) Normal force coefficient.

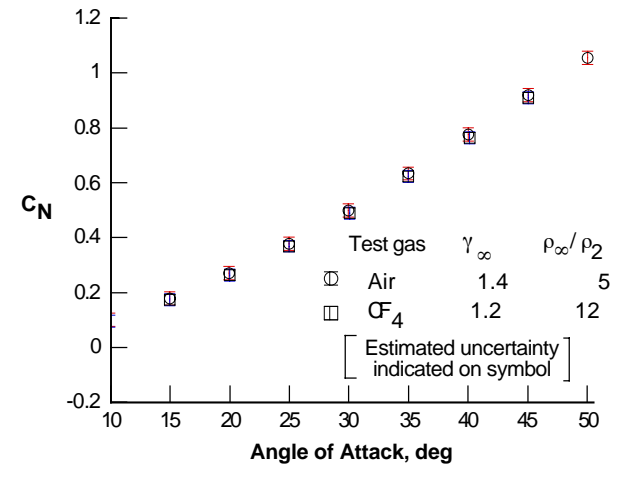


(c) Pitching moment coefficient.

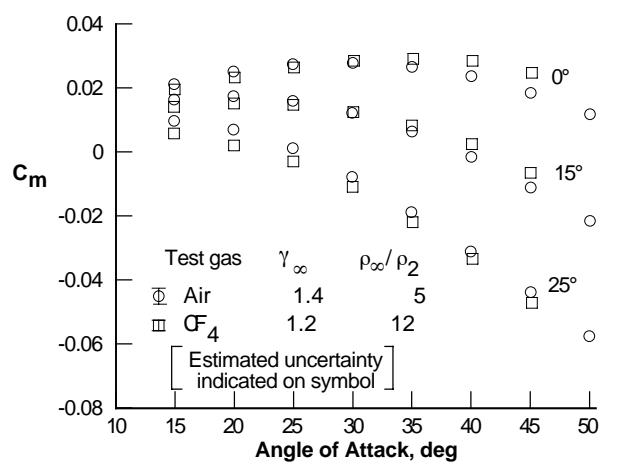


(a) Axial force coefficient.

Fig. 9. Gamma (γ) effects on X-38 Rev 3.1 longitudinal aerodynamics $M_\infty = 6$, $Re_{\infty, L} = 0.25 \times 10^6$, $\delta_{BF} = 15$ deg.



(b) Normal force coefficient.



(c) Pitching moment coefficient.

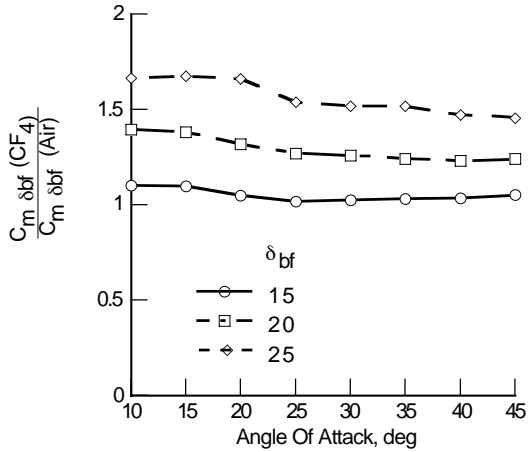
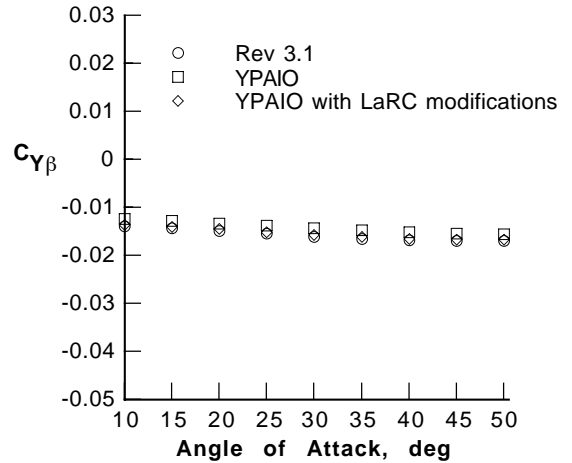
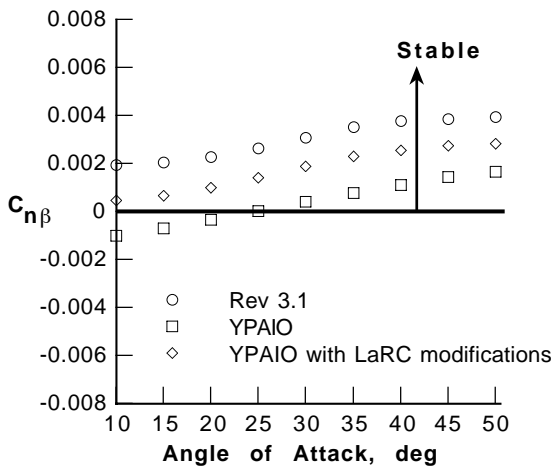


Fig. 10. Effect of gamma (γ) on X-38 Rev 3.1 body flap effectiveness $Re_{\infty, L} = 0.25 \times 10^6$.

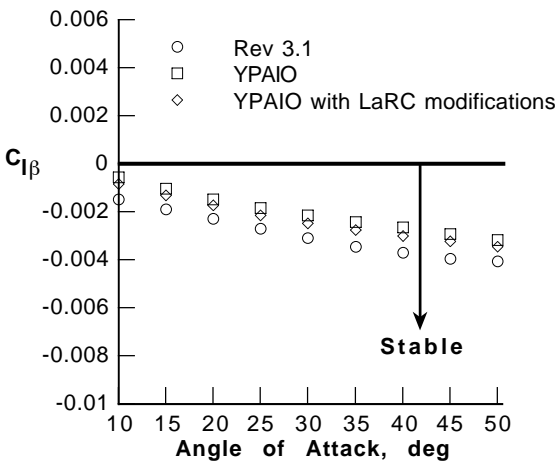


(c) Side force derivative.

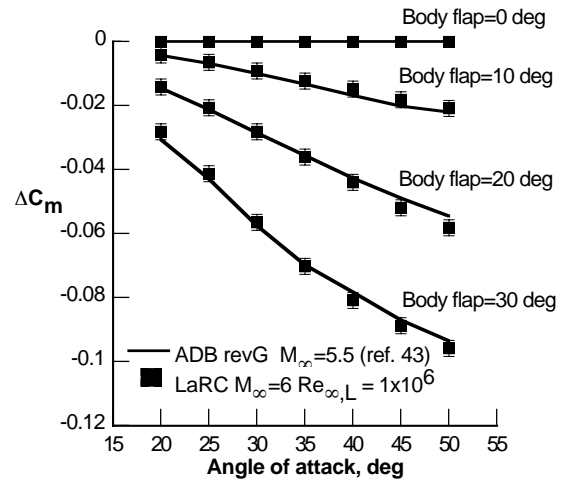


(a) Yawing moment derivative.

Fig. 11. Configuration effects on X-38 lateral/directional aerodynamics $M_{\infty} = 6$ air $Re_{\infty, L} = 0.25 \times 10^6$, $\delta_{BF} = 0$ deg $\beta = 0, \pm 2$ deg.

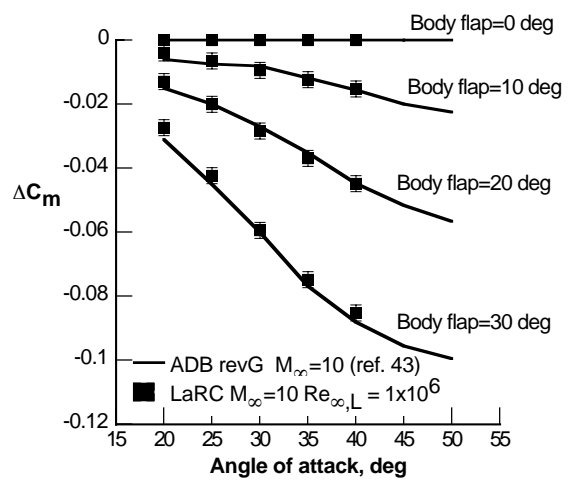


(b) Rolling moment derivative.



(a) $M_{\infty} = 6$ air.

Fig. 12. Comparison of X-38 Rev 8.3 pitching moment increments with X-38 preflight aerodynamic data book, Rev G (ref. 43).



(b) $M_{\infty} = 10$ air.

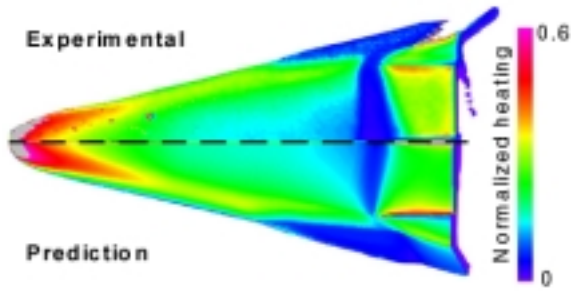
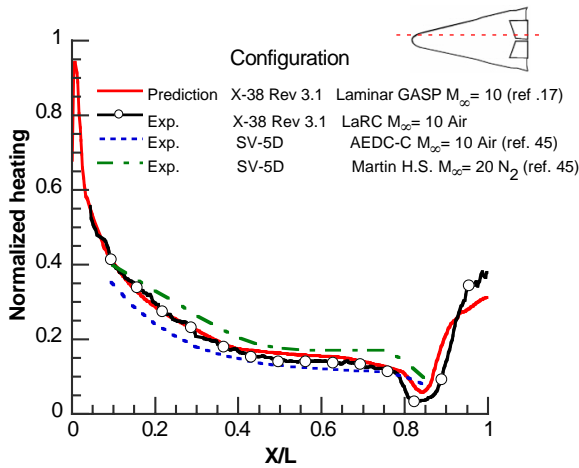
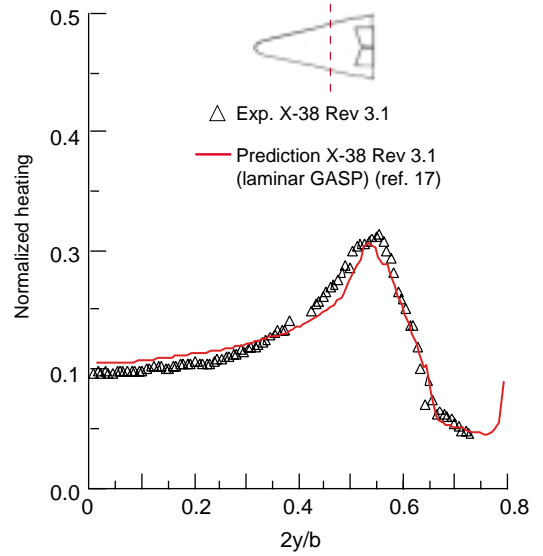


Fig 13. Comparison of measured X-38 Rev 3.1 global windward heating with laminar prediction (ref. 17)
 $M_\infty = 10$, $\alpha = 40$ deg, $\delta_{BF} = 25$ deg, $Re_{\infty, L} = 0.5 \times 10^6$.



(a) Windward centerline.

Fig. 14. Comparison of measured X-38 Rev 3.1 and SV-5D (ref. 45) heating distributions with laminar prediction (ref. 17)
 $M_\infty = 10$, $\alpha = 40$ deg, $\delta_{BF} = 25$ deg, $Re_{\infty, L} = 0.5 \times 10^6$.



(c) Axial station, $X/L = 0.73$, $M_\infty = 10$ Air.

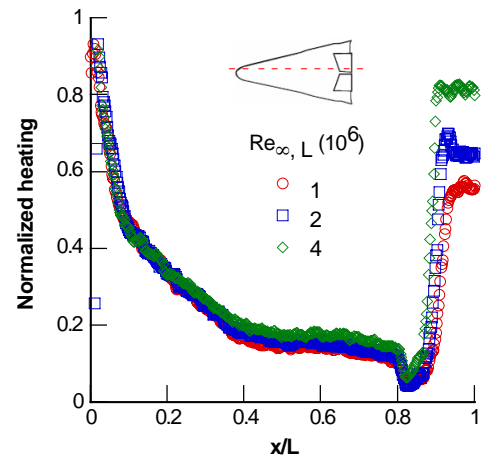
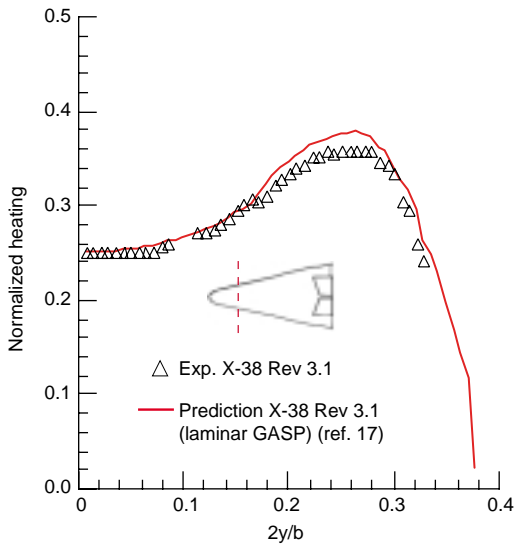


Fig. 15. Effect of Reynolds number on Rev 3.1 windward centerline heating distribution
 $M_\infty = 6$ Air, $\alpha = 40$ deg, $\delta_{BF} = 25$ deg.



(b) Axial station, $X/L = 0.25$ $M_\infty = 10$ Air.

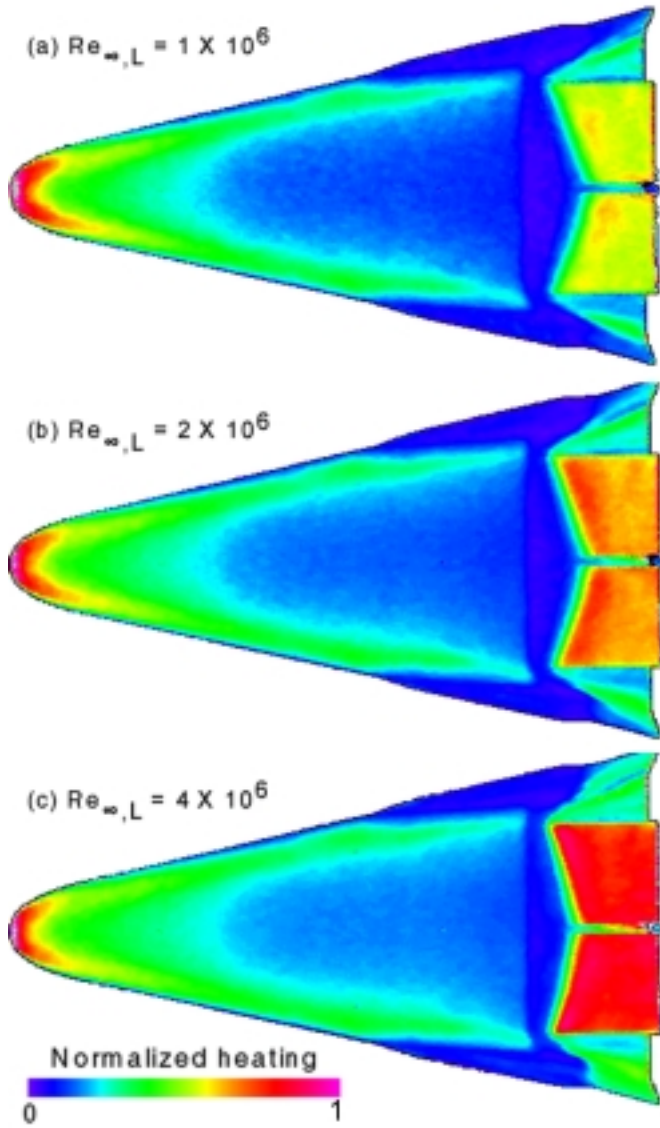


Fig. 16. Effect of Reynolds number on Rev 3.1 global windward heating.
 $M_{\infty} = 6$ Air, $\alpha = 40$ deg, $\delta_{BF} = 25$ deg.

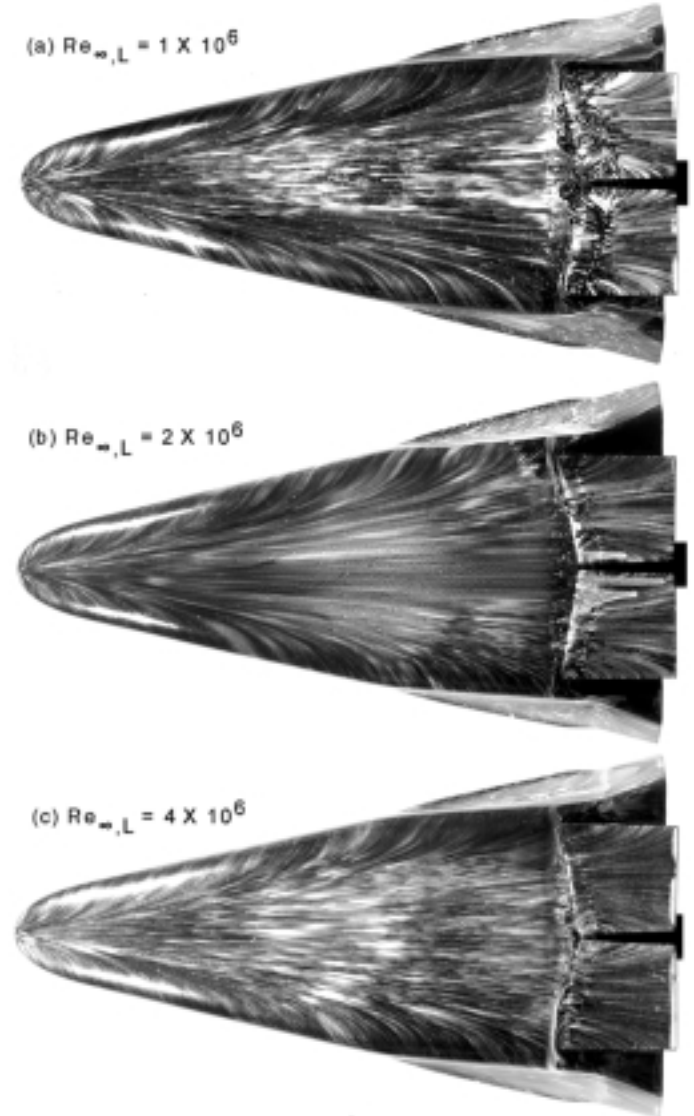


Fig. 17. Effect of Reynolds number on Rev 3.1 windward surface streamlines.
 $M_{\infty} = 6$ Air, $\alpha = 40$ deg, $\delta_{BF} = 25$ deg.

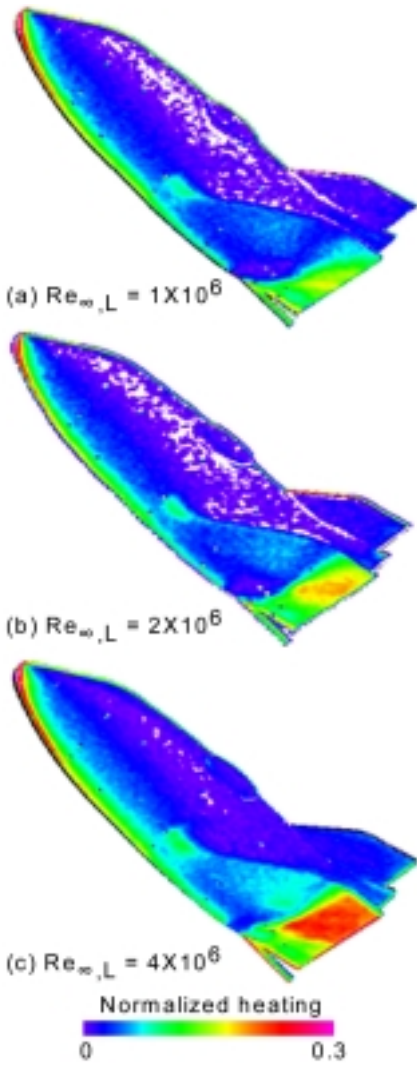


Fig. 18 Effect of Reynolds number on Rev 8.3 fin/rudder global heating $M_\infty = 6$ Air, $\alpha = 40$ deg, $\delta_{BF} = 20$ deg.

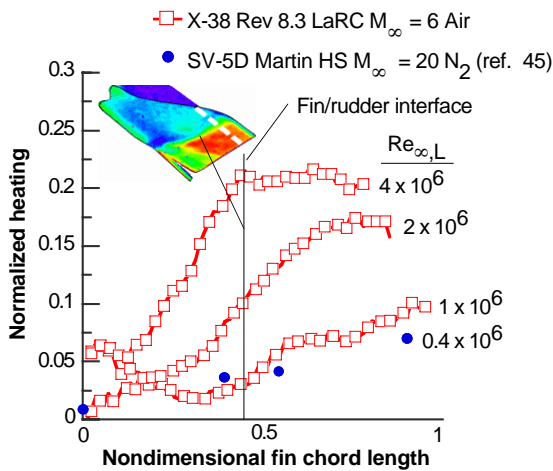


Fig. 19. Effect of Reynolds number on X-38 Rev 8.3 fin/rudder heating distribution and comparison with SV-5D (ref. 45) $M_\infty = 6$ Air, $\alpha = 40$ deg, $\delta_{BF} = 25$ deg.

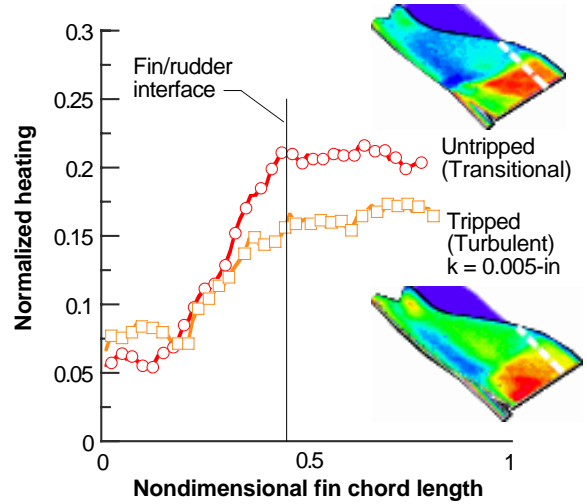


Fig. 20. Effect of Reynolds number on X-38 Rev 8.3 fin/rudder chordwise heating distribution $M_\infty = 6$ Air, $\alpha = 40$ deg, $Re_{\infty, L} = 4 \times 10^6$, $\delta_{BF} = 25$ deg.

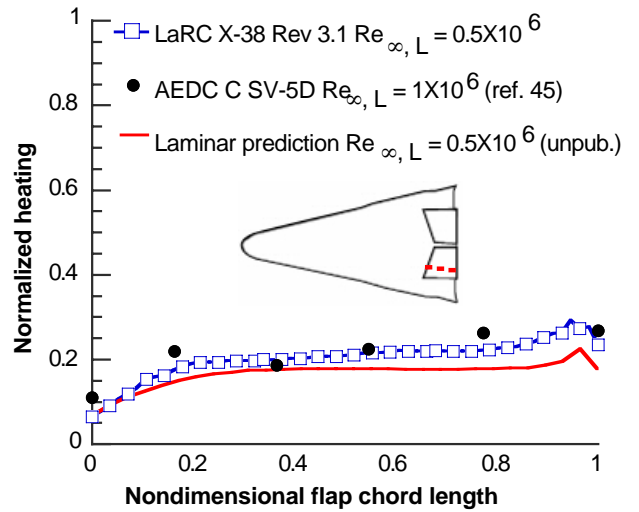


Fig. 21. Comparison of measured X-38 Rev 3.1 and SV-5D (ref. 45) body flap heating distribution with laminar prediction (unpublished) $M_\infty = 10$ Air, $\alpha = 40$ deg, $\delta_{BF} = 20$ deg.

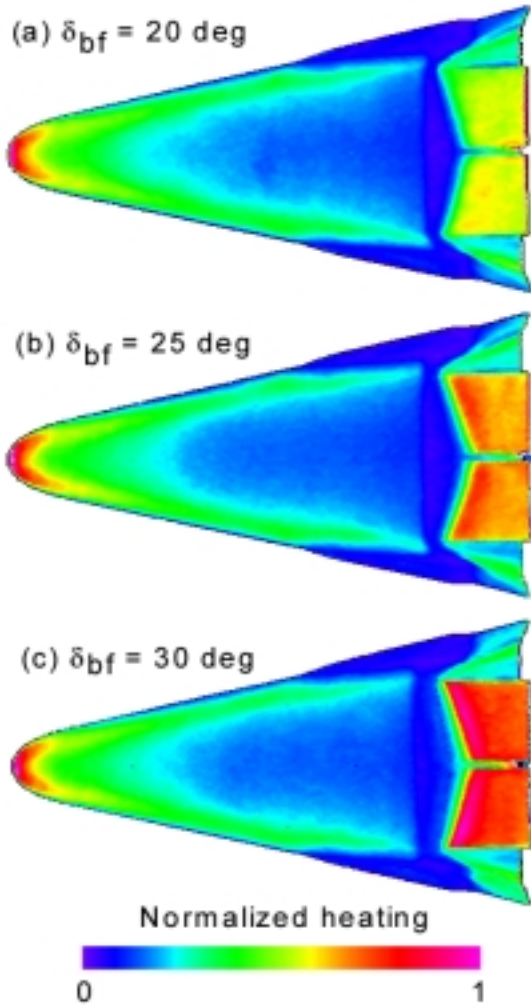


Fig. 22. Effect on body flap deflection on Rev 3.1 global windward heating
 $M_\infty = 6$ Air, $\alpha = 40$ deg, $Re_{\infty, L} = 2.0 \times 10^6$.

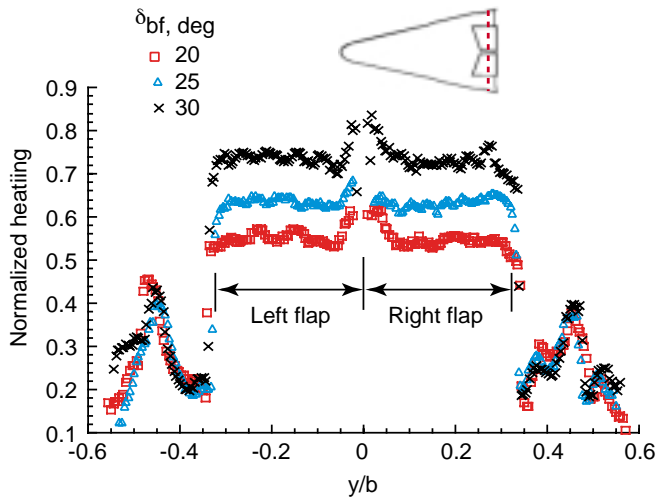


Fig. 23. Effect on body flap deflection on Rev 3.1 flap span heating distribution at $X/L = 0.98$
 $M_\infty = 6$ Air, $\alpha = 40$ deg, $Re_{\infty, L} = 2.0 \times 10^6$.

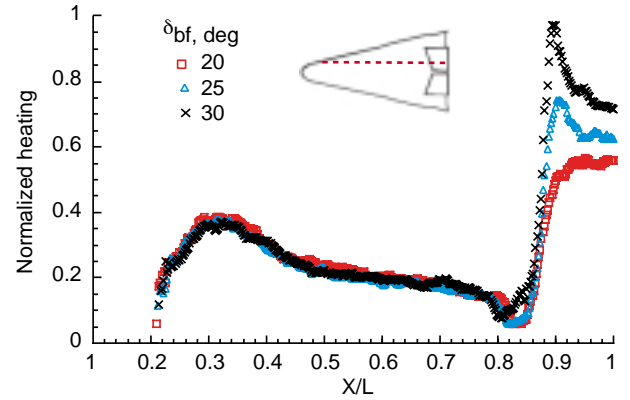


Fig. 24. Effect on body flap deflection on Rev 3.1 longitudinal heating distribution at $y/b = 0.2$
 $M_\infty = 6$ Air, $\alpha = 40$ deg, $Re_{\infty, L} = 2.0 \times 10^6$

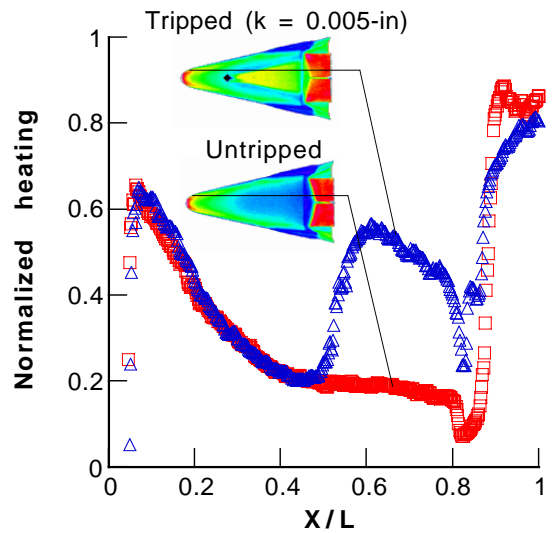
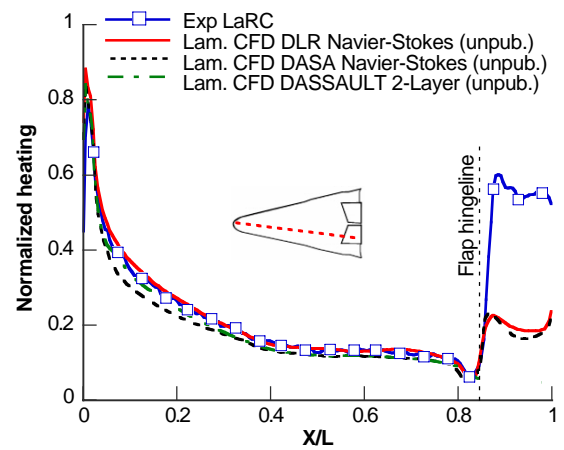


Fig. 25. Effect of boundary layer trip on X-38 Rev 3.1 longitudinal body flap heating distribution
 $M_\infty = 6$ Air, $\alpha = 40$ deg, $Re_{\infty, L} = 4 \times 10^6$, $\delta_{BF} = 25$ deg.



(a) Laminar.

Fig. 26. Comparison of measured X-38 Rev 8.3 body and flap longitudinal heating distribution with prediction (ref. 51)
 $M_\infty = 6$ Air, $\alpha = 40$ deg, $Re_{\infty, L} = 4 \times 10^6$, $\delta_{BF} = 20$ deg.

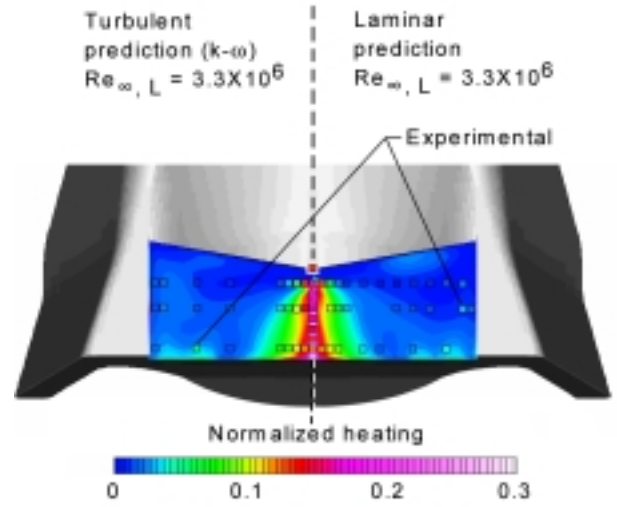
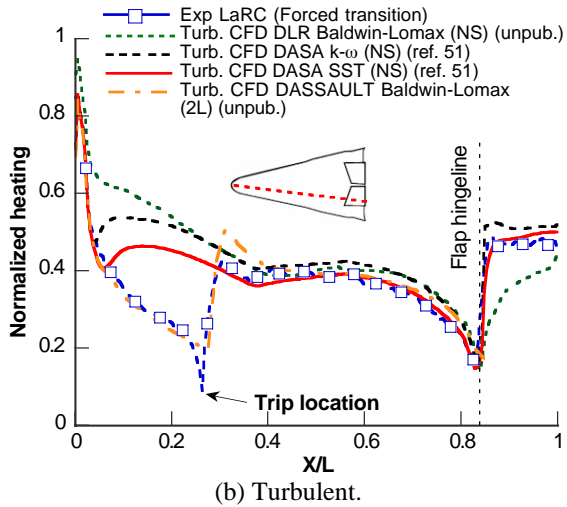


Fig.29 Comparison of discrete thin film experimental cavity floor heating with laminar and turbulent prediction (unpub.)
 $M_\infty = 6$ Air, $Re_{\infty, L} = 4 \times 10^6$, $\delta_{BF} = 20$ deg.

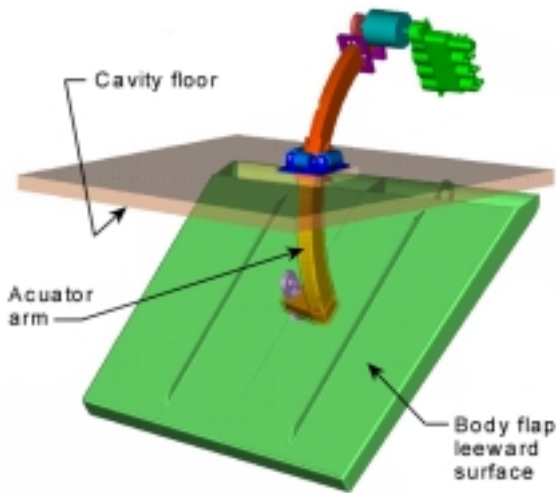


Fig. 27 X-38 Rev 8.3 flap cavity and actuator arm location (second flap omitted for clarity).

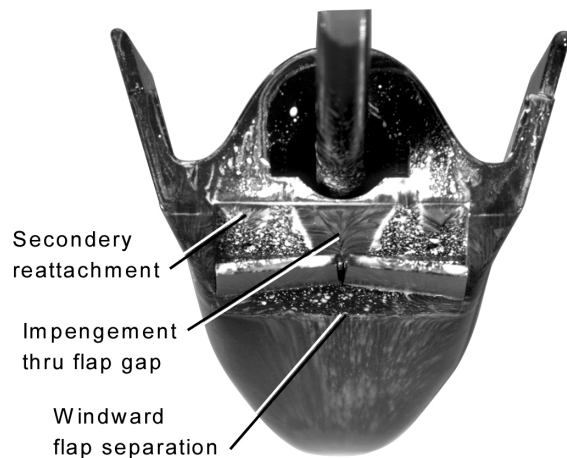


Fig. 28 X-38 rev 8.3 surface streamlines on flap cavity floor
 $M_\infty = 6$ Air, $\alpha = 40$ deg, $Re_{\infty, L} = 2.0 \times 10^6$, $\delta_{BF} = 20$ deg.

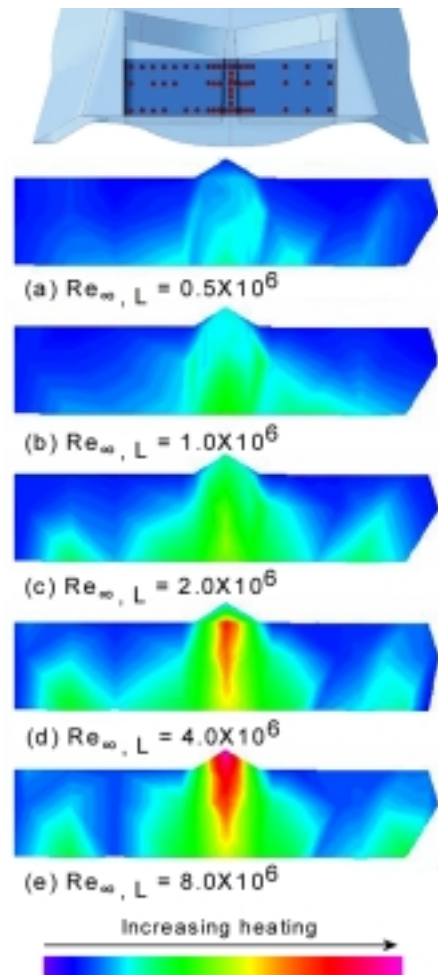


Fig 30. Effect of Reynolds number on X-38 Rev 8.3 measured cavity floor heating
 $M_\infty = 6$ Air, $\alpha = 40$ deg, $\delta_{BF} = 25$ deg.

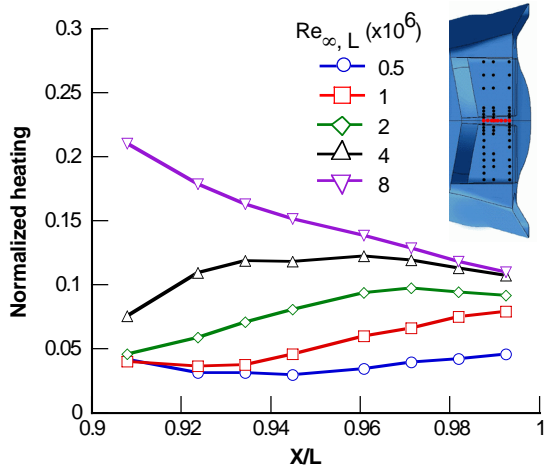


Fig 31. Effect of Reynolds number on X-38 Rev 8.3 centerline cavity floor heating distribution
 $M_\infty = 6$ Air, $\alpha = 40$ deg, $\delta_{BF} = 25$ deg.

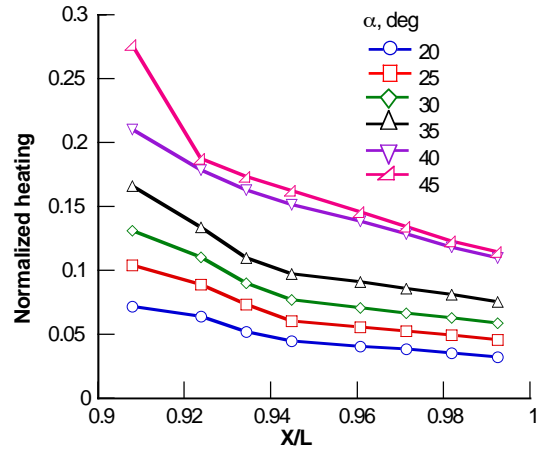


Fig 34. Effect of angle-of-attack on X-38 Rev 8.3 centerline cavity floor heating distribution
 $M_\infty = 6$ Air, $Re_{\infty, L} = 8 \times 10^6$, $\delta_{BF} = 25$ deg..

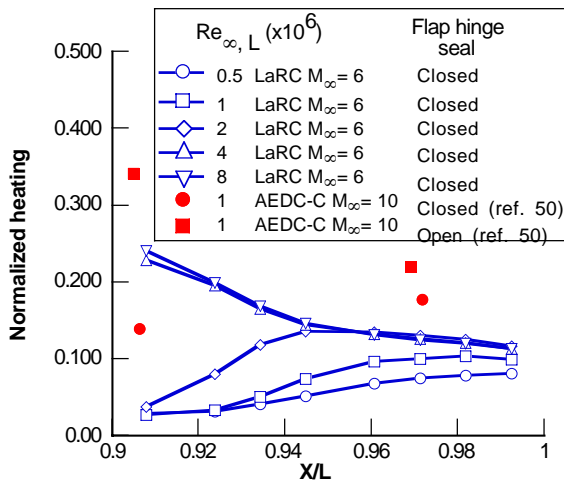


Fig 32. Comparison of measured X-38 Rev 8.3 and SV-5D (ref.50) centerline cavity floor heating distribution
 $M_\infty = 6$ Air, $\alpha = 40$ deg, $\delta_{BF} = 20$ deg.

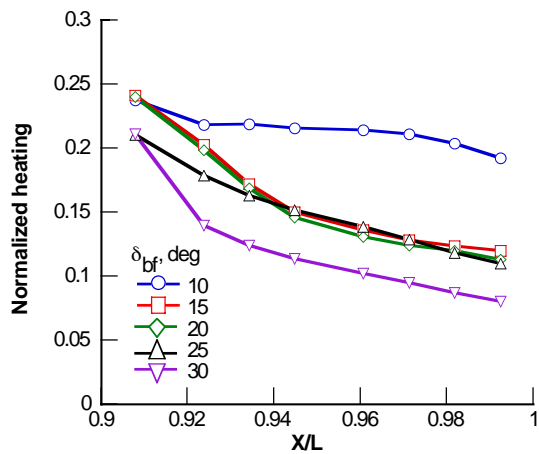


Fig 33. Effect of body flap deflection on X-38 Rev 8.3 centerline cavity floor heating distribution
 $M_\infty = 6$ Air, $\alpha = 40$ deg, $Re_{\infty, L} = 8 \times 10^6$.

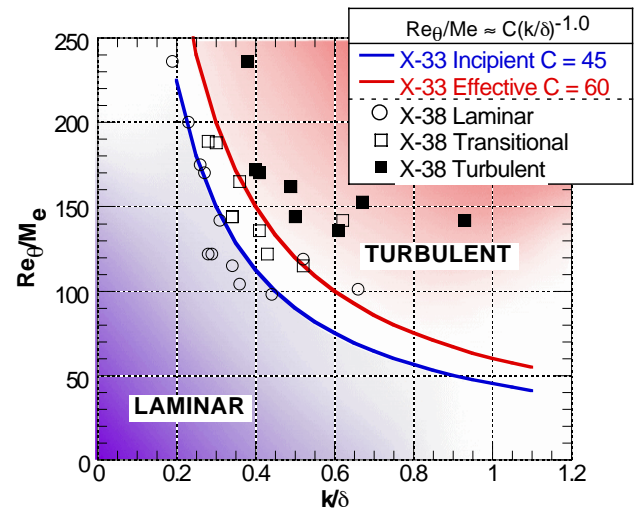
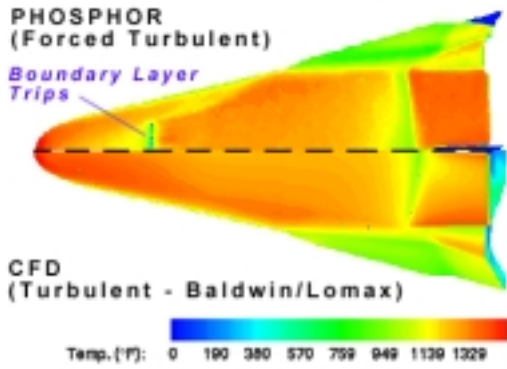
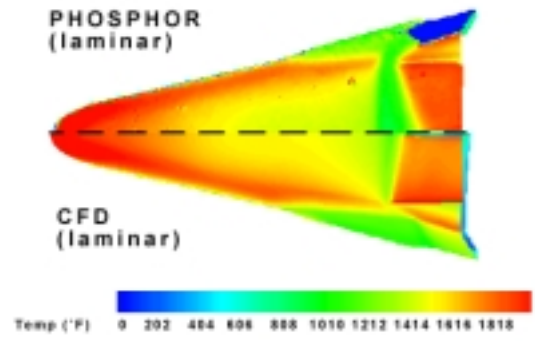


Fig 35. Experimental transition correlation of X-38 Rev 3.1 windward centerline discrete roughness data and comparison with X-33 results (ref. 53)
 $M_\infty = 6$ Air, $\alpha = 40$ deg



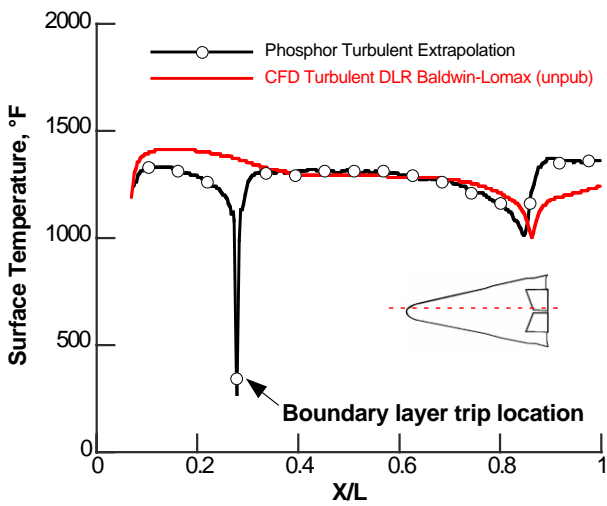
(a) Global surface temperature mapping

Fig 36. Comparison of extrapolated turbulent experimental data with turbulent flight prediction (unpublished)
 $M_\infty = 6$, $\alpha = 40$ deg, $\delta_{BF} = 20$ deg, $Re_{\infty, L} = 5 \times 10^6$.

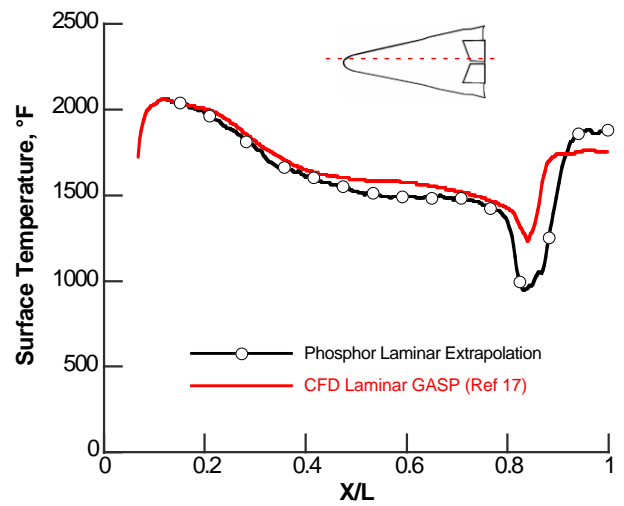


(a) Global surface temperature mapping

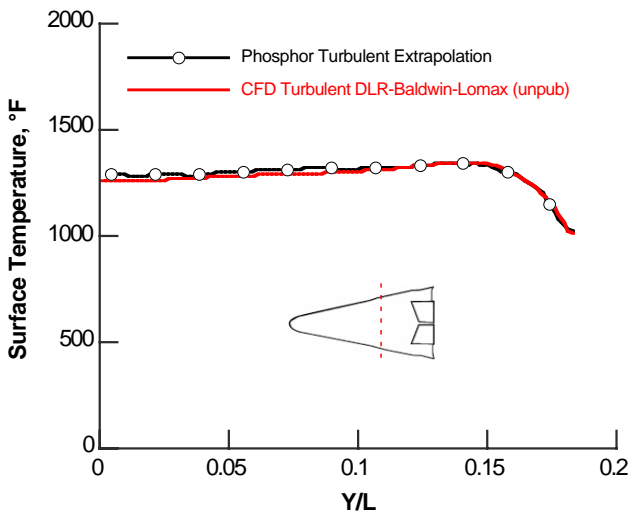
Fig 37. Comparison of extrapolated laminar experimental data with laminar flight prediction (unpublished)
 $M_\infty = 10$, $\alpha = 40$ deg, $\delta_{BF} = 25$ deg, $Re_{\infty, L} = 5 \times 10^6$.



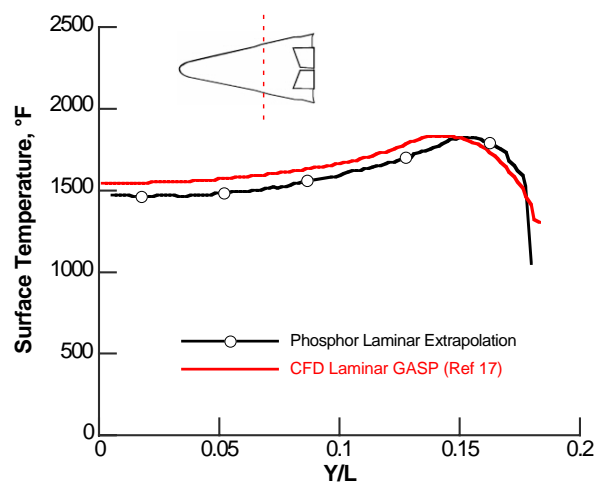
(b) Longitudinal station, $Y/L = 0.06$.



(b) Longitudinal station, $Y/L = 0.06$.



(c) Axial station, $X/L = 0.58$.



(c) Axial station, $X/L = 0.58$.